

Ngoc Thi Bich Nguyen

High-Q bulk acoustic wave resonators for RF filter applications





Ngoc Thi Bich Nguyen

**High-Q bulk acoustic wave resonators
for RF filter applications**

A PhD dissertation in
Applied Micro- and Nanosystems

© Ngoc Thi Bich Nguyen 2019

Faculty of Technology, Natural Sciences and Maritime Sciences

University of South-Eastern Norway

Borre, 2019

Doctoral dissertations at the University of South-Eastern Norway no. 24

ISSN: 2535-5244 (print)

ISSN: 2535-5252 (online)

ISBN: 978-82-7860-346-8 (print)

ISBN: 978-82-7860-347-5 (online)

This publication is licensed with a Creative Commons license. You may copy and



redistribute the material in any medium or format. You must give appropriate credit, provide a link to the license, and indicate if changes were made.

Complete license terms at

<https://creativecommons.org/licenses/by-nc-sa/4.0/deed.en>

Print: University of South-Eastern Norway

Preface

This doctoral thesis is submitted in partial fulfillment of the requirements for the degree of Philosophiae Doctor at the Faculty of Technology, Natural Sciences and Maritime Sciences, University of South-Eastern Norway (USN), Norway.

The present work was carried out at the Department of Microsystems, University of South-Eastern Norway, Norway under the supervision of Prof. Ulrik Hanke, USN, Assoc. Prof. Agne Johannessen, USN, and Dr. Stig Rooth, Kongsberg Norspace AS.

The project was mainly funded by a PhD grant from the University of South-Eastern Norway. Part of the experimental work for this project was funded by the Norwegian PhD Network on Nanotechnology for Microsystems (NanoNetwork). The experimental work was also partly funded by the European Cooperation in Science and Technology (COST) for Short-Term Scientific Missions (STSM) program.

The simulation work was partly supported by the University of Oslo and the Norwegian Metacenter for High Performance Computing under Grant NN9344K.

Acknowledgements

I would like to express my sincere gratitude to my main supervisor Prof. Ulrik Hanke for his wholehearted support during this project. His patience and helpful advice kept me constantly engaged with my research. He has been such a great mentor to me on my path to self-improvement as a scientist. I also would like to thank my co-supervisors, Assoc. Prof. Agne Johannessen and Dr. Stig Rooth, for all their guidance and fruitful discussions without which this work would have been impossible. Especially, I am grateful for Agne's company not only as a technical supervisor but also as a friend to whom I can confide.

I am grateful for the supervision of Prof. Enrique Iborra and his group during my time at his laboratory at the Technical University of Madrid (UPM). Although the collaboration for my experimental work at the UPM was short-term, I was warmly welcomed and treated as a member of his team. Thank you for your generosity and tolerance during my work and stay.

A special thanks to Zekija Ramic for training me in the clean room of the University of South-Eastern Norway (USN) before I conducted my experiments at the UPM. Thanks also to Øystein Johansen at Kongsberg Norspace for helping me set up the measurements for my device samples in the company lab. My gratitude also goes to Richard Nelson for correcting the grammar mistakes in this thesis.

My deep gratitude to the professors, lab engineers, coordinators, researchers, and friends at the Department of Microsystems, USN. Your company and assistance during this journey of mine are highly appreciated.

Most importantly, my warmest thanks to my family for their unconditional love, support, and encouragement. With them always being there for me, I could be courageous and undaunted in taking on this challenge. I am forever indebted to my parents who have given me invaluable education and motivation. This milestone would not have been possible had it not been for my family, and to them I dedicate this thesis.

Abstract

This thesis proposes a novel design method for optimizing bulk acoustic wave (BAW) resonators, including film bulk acoustic resonators (FBAR) and solidly mounted resonators (SMR). The purpose is to enhance their quality factors Q at the frequencies of interest. These resonators are targeted for the filters in the radio frequency (RF) front-end module of mobile devices. The significant losses at such high frequencies make the optimization more challenging. In the present work, acoustic loss induced by lateral leakage of Lamb waves in an FBAR or generalized Lamb waves in an SMR is alleviated to obtain a high Q factor at its antiresonance frequency. This is done by systematically modifying the resonator geometry. A dual-step frame placed atop the periphery region of a resonator serves as a lateral Bragg reflector. Each step of this frame is considered as a “mirror layer” of the reflector. Laterally propagating waves once encountering this reflector bounce back into the resonator. These waves are inhibited from escaping to the outside area and their energy is thus confined within the resonator’s active region. The key feature of the proposed frame is its ability to reflect the two wave modes that carry the largest energy. Accordingly, the step widths are calculated by means of the diffraction grating method that was previously recommended for the Bragg reflector of an SMR in literature. The step heights are estimated so that sufficient acoustic impedance mismatches are created between the non-frame regions and the step, and between the two steps. Since these computations require insight about lateral waves propagating in a BAW resonator, the characteristics of these waves in a mixed-multilayer stack of non-piezoelectric and piezoelectric materials are studied. Both Finite element method (FEM) simulations and matrix methods are utilized to determine the phase velocities of the waves, mode shapes, energy carried by each mode and acoustic impedance of each resonator region. FEM simulations are then used to evaluate the operation and performance of all the designed resonators.

The inclusion of more filters in modern RF front-end modules with limited areas suggests the device miniaturization. The impact of a reduced area on the working frequencies and performance of BAW resonators is thus investigated. As the area shrinks, the significance of lateral edge contribution to the main resonance is more prominent. The effects of a micro variation in the resonator area on its Q factor

at antiresonance frequency are also determined. This finding provides an essential guideline to designing the resonators using 2D FEM simulations.

The SMR-type resonators of three different non-framed designs are fabricated and measured to demonstrate the impact of a resonator size and shape on its performance. The (vertical) Bragg reflectors of these SMRs are designed to reflect both longitudinal and shear waves. The samples are fabricated in a consecutive sequence so that the later one can overcome the problems faced by its former one.

List of papers omitted from online edition due to publisher's restrictions

Papers included in the thesis

1. **N. Nguyen**, A. Johannessen, S. Rooth, and U. Hanke, “A design approach for high-Q FBARs with a dual step frame”, *Transactions on Ultrasonics Ferroelectrics and Frequency Control*, vol. 65, 2018, pp. 1717–1725.
2. **N. Nguyen**, A. Johannessen, S. Rooth, and U. Hanke, “The impact of area on BAW resonator performance and an approach to device miniaturization”, accepted to be published in *Ultrasonics* journal.
3. **N. Nguyen**, S. Rooth, A. Johannessen, and U. Hanke, “Improvement of methods in analyzing the propagation of plate waves in FBARs” in 2016 IEEE International Frequency Control Symposium (IFCS), 2016, pp. 1–6.
4. **N. Nguyen**, A. Johannessen, and U. Hanke, “Design of high-Q thin film bulk acoustic resonator using dual-mode reflection” in 2014 IEEE International Ultrasonics Symposium, 2014, pp. 487–490.
5. **N. Nguyen**, S. Rooth, A. Johannessen, and U. Hanke, “Geometrically optimized FBAR elements for ladder type filter”, proceeding of International Workshop on Microwave Filters, CNES/ESA, 2015.

The present work was also presented at the following workshops and seminars (without proceedings)

6. **N. Nguyen**, S. Rooth, A. Johannessen, and U. Hanke, “Inhibiting laterally leaking Lamb waves in thin film bulk acoustic resonators”, presented at Scandinavian Symposium on Physical Acoustics, Geilo, 2018.
7. **N. Nguyen**, A. Johannessen, S. Rooth, and U. Hanke, “The effects of area on the performance of solidly mounted resonators”, presented at IC1208 MCM7 & WG meeting, Luxembourg, 2017.
8. **N. Nguyen**, A. Johannessen, S. Rooth, and U. Hanke, “A new design method for the improvement of FBAR quality factor at anti-resonance frequency”, presented at IC1208 MCM7 & WG meeting, Vilnius, 2016.

Abbreviations

2D, 3D	Two-dimensional, three-dimensional
2G, 3G, 4G, 5G	The 2 nd , 3 rd , 4 th , 5 th generation of mobile technology
ABR	Acoustic Bragg reflector
BAW	Bulk acoustic wave
BC	Boundary condition
CA	Carrier aggregation
CAGR	Compound annual growth rate
DFT	Discrete Fourier transform
DGM	Diffraction grating method
EM	Electromagnetic
FBAR	Thin film bulk acoustic resonator
FEM	Finite element method
GM	Global matrix
IC	Integrated circuit
IDT	Interdigital transducer
LTE	Long-term evolution
MIMO	Multiple input multiple output
R-L	Rayleigh–Lamb
RF	Radio frequency
Rx	Receiver

SAW	Surface acoustic wave
SH	Horizontal shear
SMR	Solidly mounted resonator
STM	Stopband theory method
SVD	Singular value decomposition
SV	Vertical shear
TCF	Temperature coefficient of frequency
TE	Thickness extension
TM	Transfer matrix
Tx	Transmitter
UHF	Ultra high frequency
VHF	Very high frequency
mBVD	Modified Butterworth van Dyke
q-L	Quasi-longitudinal
q-SH	Quasi-horizontal shear
q-S	Quasi-shear
q-SV	Quasi-vertical shear

Contents

Preface	i
Acknowledgements	iii
Abstract	v
List of papers	vii
Abbreviations	ix
1 Introduction	1
1.1 Bulk acoustic wave resonators and filters — a history	1
1.2 Motivation	4
1.3 Challenges	13
1.4 Objectives	14
2 Propagation of lateral acoustic waves in BAW resonators	16
2.1 Lamb waves in an isotropic plate	16
2.2 Transfer matrix (TM) method	20
2.3 Global Matrix method	26

2.4	Testing the methods	28
3	Design of high-Q BAW resonators using dual-step frame method	34
3.1	Acoustic Bragg reflector (ABR)	34
3.1.1	Conventional ABR	34
3.1.2	Dual-wave-reflected ABR	35
3.1.3	Dual-step frame method	37
3.2	Acoustic Poynting vector for piezoelectric media	39
3.3	A design guideline for high-Q BAW resonators	42
3.3.1	Material selection	42
3.3.2	Thickness optimization	43
3.3.3	Lamb wave characteristics and power flows	44
3.3.4	Frame calculation	45
3.3.5	Performance evaluation	47
3.4	High-Q BAW resonators	48
3.4.1	Designed resonators and FEM simulation setups	48
3.4.2	Simulation results	50
3.4.3	Side effects	50
4	The impact of area on BAW resonator performance	53
4.1	Resonance and antiresonance frequencies affected by transverse behavior of the TE_1 mode	53
4.2	Influence of area on resonator performance	56

4.2.1	Background	56
4.2.2	FBARs	56
4.2.3	SMRs	58
4.2.4	k_{eff}^2 factor of the miniaturized resonators	58
4.2.5	Impact of material quality	59
4.3	Microfabrication of the non-framed SMRs	60
4.3.1	The designed SMRs	60
4.3.2	Experimental setups and sample preparation	60
4.3.3	Measurement results	61
5	Conclusions and prospects	64
5.1	Conclusions	64
5.2	Prospects	67
	Bibliography	69
	Papers	81

Chapter 1

Introduction

1.1 Bulk acoustic wave resonators and filters – a history

The prosperous era of RF bulk acoustic wave (BAW) resonators using piezoelectric thin films and their filters began in the early eighties when they were first introduced by Grudkowski et al. [1] and Lakin et al. [2] as a novel filter technology for very high frequency (VHF) and ultra high frequency (UHF) bands. The proposed resonators contained a thin ZnO film deposited on a thin p-doped Si membrane below which the supported Si substrate was etched to form an air hole. The resonator was electrically excited via the Al electrodes. Such a configuration can be categorized as thin film bulk acoustic resonator, known as the FBAR-type BAW resonators. The thin Si membrane was excluded in the next resonator generations, leaving a free-surface sandwiched structure of two metal electrodes and a piezoelectric layer in between (Fig. 1.1 (a)). The other category of BAW resonators is the solidly mounted resonator, or SMR type (Fig. 1.1 (b)), which was first proposed by Newell [3] and later studied by Lakin and his colleagues [4]. An overview of these resonators and their applications for filtering in their early years was also provided by Lakin [5] and later by Mahon and Aigner [6]. Both types of resonators share the

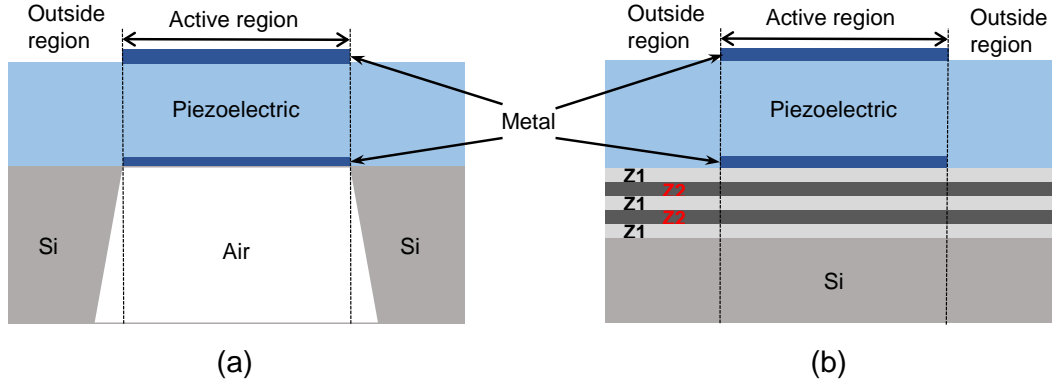


Figure 1.1: Simple 2D schematics of an FBAR (a) and an SMR (b). Figure is not drawn to scale.

same working principle based on the generation and propagation of bulk acoustic waves in piezoelectric media. That is, an electrical excitation generates longitudinal bulk waves in the piezoelectric medium with proper crystal orientation. These propagating waves are reflected back and forth in the medium, forming standing waves in the vertical direction and causing resonances. The fundamental resonance occurs when the thickness h of the piezoelectric layer equals half wavelength $\lambda_L/2$ of the longitudinal waves. The resonance frequency f_r is subsequently calculated as

$$f_r = \frac{\nu_L}{2h} \quad , \quad (1.1)$$

where ν_L is the velocity of longitudinal waves in the piezoelectric medium. This formula is only valid if the electrodes are assumed infinitely thin. In reality, due to the mechanical contribution of the electrodes, f_r holds a considerably lower value than $\nu_L/2h$. The two resonator types, however, can be distinguished based on the technique to confine acoustic waves in the piezoelectric layer. In the SMR, a stack of alternating low and high acoustic impedance layers denoted by Z1 and Z2 in Fig. 1.1 (b), is placed under the bottom electrode, atop the Si substrate. This structure is commonly known as an acoustic Bragg mirror, upon which the traveling longitudinal waves are reflected. The reflection of these waves, in the case of FBAR, is achieved by taking advantage of the large acoustic mismatch between the electrode materials and air at both upper and lower surfaces. This means an air-gap cavity or a hole has to

be etched below the bottom electrode of the resonator. A bandpass radio frequency (RF) filter is created from two or more of such BAW resonators by configuring them in various filter topologies such as ladder, stack, balanced bridge, lattice [7]. Two filters, one used for transmitting (transmitter – Tx) and another used for receiving (receiver – Rx) signal in the same band together construct the so-called duplexer found in many communication systems. A quadplexer is formed by the integration of two transmitters and two receivers, i.e. four filters, in the multiport module. Other multiplexers of which resonators are the core building blocks are constructed in a similar fashion.

The inventive combination of thin film technology and acoustic resonators has become the foundation for a generation of sophisticated RF filters. Acoustic waves propagate at velocities of about 4–5 orders lower, and thus much shorter wavelengths, than those of electromagnetic (EM) waves. This implies a great advantage of acoustic wave resonators over EM wave resonators operating in the RF range up to 10 GHz in terms of physical size, power consumption, and circuit integration [8], [9]. More importantly, acoustic wave resonators provide low insertion loss and good performance. They meet the requirements of modern wireless communication systems especially when portability and compactness of the devices are demanded. Filters based on surface acoustic wave (SAW) resonators, due to this reason, have been widely used in mobile telephony since the dawn of cellular phones about 20 years ago [10]. BAW filters were then developed and commercialized as a competitor of SAW filters in 2001 [11]. SAW filters are capable of providing small size devices with high performance, tolerable insertion loss and good rejection up to 1.5 GHz. However, for frequencies beyond 2 GHz, they no longer fulfill the demands of insertion loss, passband skirt steepness and power handling of the wireless applications. In addition to the degradation of electrical performance, they are highly sensitive to temperature variation and more challenging to fabricate because the interdigital transducers (IDTs) need much narrower electrodes. BAW filters and multiplexers, as reported in literature [10], [12–14], are a promising replacement of their SAW

counterparts for the range above 2 GHz. They surpass SAW filters and are gradually taking over the filtering market for high frequency range. Even though the market continues to grow rapidly, there is still no new technology that can replace them in the near future [15].

The large and potential market of BAW devices has attracted many companies into developing and becoming the vendors of BAW products on a global scale. The world has witnessed the flourishing of BAW filters and multiplexers in industry since they were first introduced by Lakin and his group at TRF Technologies. In 2001, the first FBAR duplexer developed by Ruby and his team [16] was commercialized by Agilent. In 2002, Infineon Technologies produced their SMR filters [17] in volume. TriQuint Semiconductors (the former name of the present Qovor) followed the flow with the same technology for mobile handsets. In 2005, the division of Agilent was acquired by another company, later becoming Avago Technologies. In 2008, Avago acquired Infineons BAW business, completed its BAW technology and became the leading FBAR filter and duplexer manufacturer of wireless systems. The company, after the acquisition of Broadcom in 2016, has recently changed its name to Broadcom Inc. Its top FBAR filtering technology supports more than 15 different frequency bands for Forth Generation / Long-Term Evolution (4G/LTE) applications. Also in 2005, TRF was acquired by TriQuint. The company is now one of the top vendors in the BAW market, the second only to Broadcom Inc., with its leading SMR filter products working in various bands from several hundred MHz to more than 2.6 GHz. The recent market is also shared by three other major vendors, including TDK, Skywork Solutions, and Akoustis Technologies.

1.2 Motivation

Mobile communication remains an essential part of our modern lives with the emergence of smartphone flagships, tablets, smartwatches, Bluetooth devices and other handset innovations. The number of mobile connections to the Internet reached 7

billion in 2013 and 8% of the compound annual growth rate (CAGR) in the period 2013–2018. At the same time, the demand for data rate augmented more than six-fold from 2014 to 2018 and the speed of data being transmitted in 2030 will be 5000 times the speed it was in 2011 [18], which is an exponential growth rate! The increasing demands for broadband and high data speed applications leads to the evolution of network generations (denoted by G) from 2G to 3G, 4G/LTE and the incoming 5G. The rapid growth of the whole system occurs at a time when the frequency range allocated to mobile communications is limited. Recently there are more than 45 cellular frequency bands sharing a spectrum between 700 MHz and 4 GHz and this number increases as more bands are released [19]. This has entailed a great deal of innovative terms, such as new bands, carrier aggregation (CA), multiple inputs multiple outputs (MIMO) in order to solve the overcrowding problem [20]. The increasing number of bands that a front-end module can support infers the increasing of coexisting filters in a single device. The RF front-end modules of mobile devices consequently continue to evolve in terms of complexity and integration. Indeed, the average number of RF front-end filters per each device rises from 10–12 in the year 2014 to 40–50 in 2018 and could reach 100+ by 2020 [18], [21]. These filters are squeezed into an allocated space of the mobile device that is mostly not expanded in area since the ultra-thin smartphone trend thrives and a larger battery is required for more power consumption applications. As a result, another problem is created in the front-end modules - overcrowding in terms of physical size.

With an average of 2 billion smartphones sold each year, the market is in need of 50–200 billion filters a year. For such a massive market, the filter technologies that can fulfill the requirements of these rapidly-evolving RF systems are essentially SAW and BAW filters. That means, for frequency bands above 2 GHz, BAW filters are virtually invincible. The BAW RF filter market is hence predicted to grow at 30.86% CAGR during the period 2016–2020 [22], implying a prosperous age of microacoustic filter design. The reason is that, as the systems evolve so do the BAW filters. They must fulfill more demanding criteria for selectivity, insertion

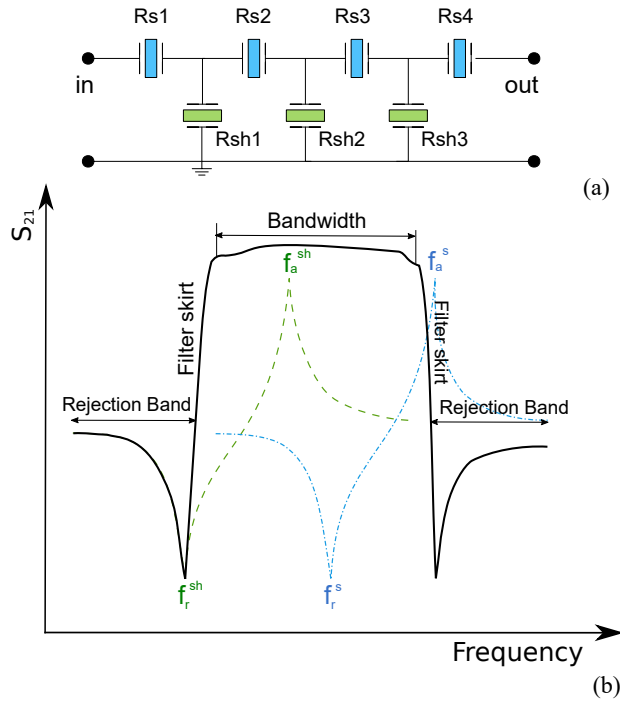


Figure 1.2: Simple 2D schematics of an FBAR (a) and an SMR (b). Figure is not drawn to scale.

loss, and bandwidth in order to provide a good isolation between Tx and Rx bands without any significant drop in the signal level. In addition, compactness and low temperature coefficient of frequency (TCF) are highly desired. This explains why BAW filter designers worldwide work intensively on the optimization of the filters, focusing on performance improvement, temperature compensation, and size and cost reduction.

Fig. 1.2 shows the sketch of a ladder filter and its response with two edges resembling a skirt. The name “filter skirt” originates from such an analogy. In order to solve the band crowding problem, high performance filters are the most desired. They can be achieved when the steepness of the filter skirts is very high, which closely relates to the high quality factors Q of the component BAW resonators. In addition, higher resonator Q can also be interpreted as lower insertion loss [23], which is also a critical factor as more and more filter units are inserted into the RF front-end modules of the mobile devices. The Q factor is defined as the ratio of the resonator total energy to the power lost in one cycle at the frequencies of interest that are

normally resonance frequency f_r and antiresonance frequency f_a . The Q factors of a resonator significantly decrease as its operating frequency increases. This implies a big challenge in designing high performance filters when their operating bands fall within the high end of LTE spectrum or even higher (e.g. 5G in the first phase will support frequencies up to 6 GHz). As a matter of fact, the Q factors of a BAW resonator rely on many factors such as material quality, resonator area and geometry, uniformity of its layers, roughness of the layer interfaces and surfaces, crystal orientation of the piezoelectric film, electromechanical coupling, electrical interconnections. The deterioration of any of these factors can be the source of loss and strongly affect the Q values, making it harder to control them altogether. These loss mechanisms in a BAW resonator were well documented in literature [7], [12], [24], [25]. Consequently, despite more than 30 years of research and development, there is still room for the improvement of Q factors and the miniaturization of the resonators working in the LTE bands and higher. The directions of research regarding such enhancement over the past decades can be summarized as follows:

- Improving the materials of the resonator piezoelectric thin film in terms of material quality factor, coupling factor, and growth techniques [26–29]. In addition to the common materials used in BAW resonators like AlN, doped AlN, ZnO, and PZT, other materials like GaN, langasite are also explored and utilized [30–33].
- Reducing acoustic loss through the Bragg mirror for SMR-type resonators with various combinations of low/high acoustic impedance materials, numbers of layers, as well as engineering the layer thicknesses for dual wave reflection [34–36].
- Modifying the resonator geometry to handle spurious modes. These modes result from the lateral resonances of Lamb waves or generalized Lamb waves propagating in the piezoelectric layer. They appear in the resonator electrical response in form of parasitic resonances (Fig. 1.3). Once occurring at or close to f_r or f_a , they consume energy at these frequencies and make the Q factors

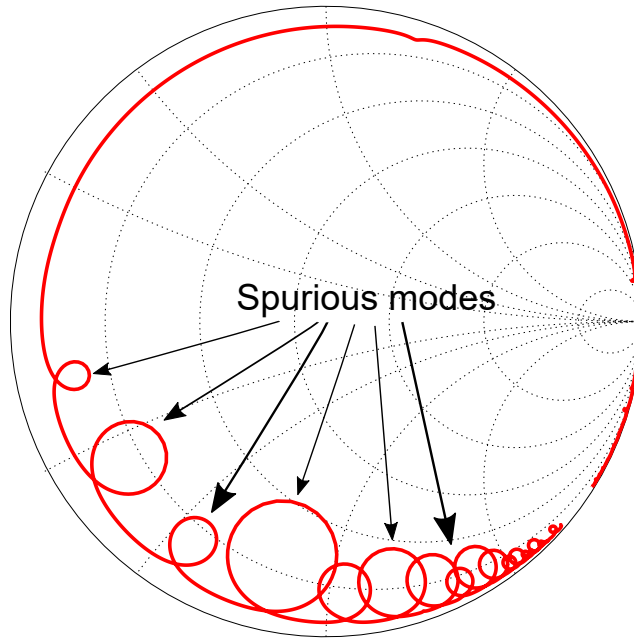


Figure 1.3: Resonator response with spurious modes on a Smith chart.



Figure 1.4: Frames in BAW resonators of type I (a) and type II (b) following the method proposed by Kaitila. The resonators are not drawn to scale.

degrade. There are two ways of modifications that can be applied either separately or combined together to obtain a better resonator response. The first method is called apodization which does not eliminate spurious modes but smears them out and creates large number of weak modes instead of a small number of strong ones [37], [38]. The resonator thus has a smoother response rather than better Q factors. The second method is to engineer a so-called frame (see, for example, Fig. 1.4) at the perimeter region of the resonator to suppress spurious modes and confine energy in the main resonance, by that enhance the Q_r factor.

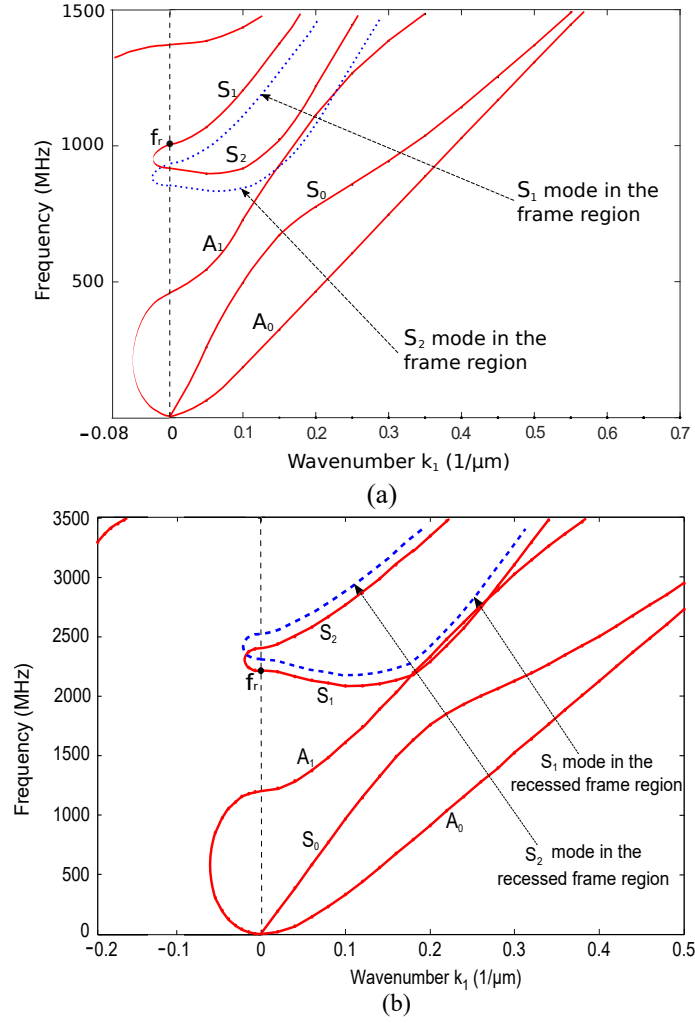


Figure 1.5: Type-I dispersion curves of a 3 μm thick ZnO plate (a) and type-II dispersion curves of a 2.5 μm thick AlN plate (b). The left parts to the vertical zero axes are plotted for imaginary values of k_1 and the right parts are for real values of k_1 .

The frame method used in recent BAW resonators was first proposed by Kaitila et al. for the SMRs [39], [40]. Another pattern of the structure for the FBAR was also granted to another group [41], [42]. Since then, the method has been widely applied for both FBARs and SMRs with different variations at many ranges of frequencies. Some of the studies on this method can be found in [7], [43–46]. The principle of the frame can be explained using a dispersion diagram of Lamb waves in a plate, which nonlinearly relates the wavenumber component in the propagating direction $k_1 = 1/\lambda_{\text{Lamb mode}}$ or wave velocity of Lamb waves to frequency. The curves seen in the diagram correspond to various modes of Lamb waves in which S_i indicates symmetric modes and A_i indicates asymmetric modes. For instance,

Fig. 1.5 shows such a diagram for a ZnO plate (which can be considered as a freely-vibrating resonator with infinitely thin electrodes). It is called a type-I dispersion, where the S_1 curve has a positive slope, or in other words, a positive group velocity (Fig. 1.5(a)). A dispersion is said of type II if the slope, or group velocity, of the S_1 mode in the vicinity of its cut-off point is negative, normally seen in AlN-based resonators (Fig. 1.5(b)). The cut-off frequency of the S_1 mode coincides with f_r of an infinitely large plate (for both types). For type-I resonator, since the S_1 mode occurs closely above f_r , lateral resonances of this mode cause strong spurious modes at these frequencies. A raised frame placed at the perimeter of the resonator, as depicted in Fig. 1.4(a), will create a region where the dispersion curves of all modes are shifted towards lower frequencies (e.g. see Fig. 1.5(a)). It means that at f_r , the wavenumber k_1 of the S_1 mode is zero in the active region (cut-off), real in the frame region, and imaginary in the outside region. Such a condition creates a uniform displacement throughout the active region, matching the constant electrical field. Hence, the spurious modes caused by the S_1 mode cannot couple with the driving field at f_r . The resonator is said to work in a “piston mode”. The theory has been verified by experimental results, showing the suppression of spurious mode in the electrical curves and flat displacement in the active area [40], [45]. For type-II resonator, a recessed frame must be used instead of a raised frame, as shown in Fig. 1.4(b). However, despite that the suppression of the S_1 mode and an amount of improvement in Q factors below f_r were observed, Q factors everywhere above f_r are degraded.

There are still some uncertainties remaining regarding the foregoing frame method that have not yet to be unraveled. Firstly, at f_r and f_a , there are at least four distinct propagating Lamb modes, i.e. modes with different wavelengths, in the FBAR and even larger number of lateral modes in the SMR, owing to its mirror. The frame is designed with an emphasis on suppressing the spurious resonances caused by the S_1 mode (i.e. in the FBAR case). It has not been proven that the resonances induced by rest of the Lamb modes could be alleviated with the same frame design. Secondly,

the reason this method is not efficient for type-II resonators remains unexplained. Some argue that the recessed frame acts as a lateral impedance matching layer and intensifies the transmission and thus the leakage of Lamb waves to the outside region of the resonator [7]. This matching principle is commonly seen in medical ultrasound transducers, utilized to maximize the transmission of sound waves from the piezoelectric material to the tissues [47]. If this is the case, the lateral leakage of Lamb waves might outweigh the loss induced by spurious modes and should be the focus of interest in enhancing the Q factors of the resonator.

It is reported that an application of a raised frame contiguous to a recessed frame in a type-II resonator [7], [44] has improved the Q factors, far better than those of a resonator with only a recessed frame. The “optimal” width of such a raised frame is found to be quarter wavelengths of the S_1 mode. The principle of such a frame combination can be elaborated as follows: it is well known that in high-reflection optical coating, an alternate combination of low and high index quarter-wavelength layers, also known as a dielectric mirror or a Bragg reflector, can reflect incoming light. An analogue of this mechanism can be made for acoustic waves. The recessed and raised frames serve as low and high impedance quarter-wavelength layers, also known as a lateral Bragg mirror pair, for the reflection of the S_1 mode. In [48], a repetition of recessed and raised frames in the lateral dimension is reported to further increase the Q factors. It seems to be a reasonable enhancement since the reflection coefficient of a Bragg reflector raises with its number of mirror pairs [49]. However, in this design, the width of the first recessed frame is calculated according to the theory of piston mode (so not following the Bragg’s law) while the rest of the frame widths are selected by simultaneously sweeping along the widths of the recessed and raised frames to look for the combination that results in the highest Q values. That is, no specific design guideline were provided for these frames. The whole frame structure thus might not entirely function as an effective Bragg reflector with multiple mirror pairs.

Surprisingly, the experimental results presented in [7] show that a type-II resonator

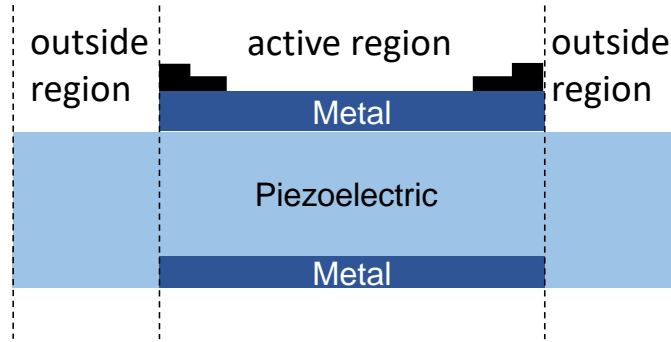


Figure 1.6: The proposed frame structure for high-Q BAW resonators.

with only a raised frame provides even better Q factors than does the one with both recessed and raised frames. This implies the large impact of inhibiting lateral leakage as well as the critical role a well-constructed lateral Bragg reflector plays in achieving a high- Q resonator. In the previous work [7], [40], [44], [48], only the mode S_1 is taken into consideration since this mode is the larger contributor to loss (as compared to the S_0 mode). Other A_i modes are not considered mostly because they are flexure modes and cannot be electrically measured like those S_i modes. However, it will be shown later in Chapter 3 that the acoustic energy the A_1 mode carries is comparable to the energy carried by S_1 . It means the contribution of A_1 to the total loss should not be ignored. All of these arguments become the inspiration for a new design principle and guideline for high performance BAW resonators as a counterpart of the aforementioned piston method. That is, a multi-step frame (Fig. 1.6) is constructed as a lateral Bragg mirror based on the acoustic impedance mismatch between the steps. The purpose of this innovative structure is to reduce the acoustic lateral leakage of multiple Lamb modes from the active region to the outside region thereby improve the performance of the next generations of BAW resonators.

1.3 Challenges

The generation and propagation of Lamb waves in BAW resonators are inevitable due to the coexistence and coupling of longitudinal and vertical shear waves at the free surfaces. The mechanism of Lamb wave formation can be explained using a transverse resonance analysis [50]. These waves are the cause for acoustic loss, spurious modes and additional ohmic loss in the electrodes, all affecting the Q factors [51]. A dispersion diagram of these waves is demanded in order to study their characteristics in the resonator. There are several methods to obtain such a diagram. The first one is to take the discrete Fourier transform (DFT) of the tracked vertical displacement in the resonator using interferometry. This method is done experimentally. The second one is to use finite element method (FEM) software to simulate the resonator, obtain the vertical component of the surface displacement to which a DFT is applied. Lamb waves in BAW resonators have the wavelengths of several microns. Resolving these waves requires an extremely fine discretization, i.e. mesh size, over a large area compared to the wavelengths. This results in bulky FEM models that demand huge computer memories and large amount of simulation time. In most cases, the models have to be reduced from 3D to 2D to deal with the issue. In return, the simulations for any shapes of the resonator rather than the square or rectangular ones cannot be conducted.

Nevertheless, the first and second methods lack details about the mode shapes and distribution of fields like strains, stresses, electrical displacements, power flow of each Lamb mode, which, in order to design an efficient frame/reflector structure, must be thoroughly understood. Fortunately, this can be done in a third way – using matrix techniques to solve the wave equations. In general, the acoustic wave problems are much more difficult to handle than electromagnetic wave problems. For a single layer of isotropic material, the equations can be solved analytically and the dispersion can be found by numerically solving the well-known Rayleigh-Lamb wave equations [50], [52]. The situation, however, is significantly more complicated

for BAW resonators. The active region of a BAW resonator is a stratified structure with piezoelectric and non-piezoelectric layers. The mixed properties of isotropy, anisotropy and piezoelectricity of the active region need to be handled by using matrix methods – an analytical-numerical hybrid way to solve such an intricate problem. Numerical errors and long calculation time are unavoidable challenges, especially when the number of layers increases. Non-dimensionalization, scaling, and matrix decomposition techniques must be also carried out in order to find the correct solutions.

The designed frame modifies the acoustic impedance of the stratified region on which it is located. All of its features including material, height, width, and number of steps in the frame have to be carefully selected and calculated. This procedure requires specific knowledge adopted from optics and transmission line theory in addition to acoustic waves and fields in solids.

The techniques for fabricating the resonators is also a big challenge since their performance depends on, inter alia, material purity, crystallinity and density, uniformity of the deposited layers, precision of layer thickness, roughness of each layer at the interfaces, and electrical parasitic components.

1.4 Objectives

In this work, Lamb waves propagating in the active regions and the frame regions of BAW resonators are characterized by the use of Transfer Matrix and Global Matrix methods and FEM simulations. The matrices of boundary conditions are modified so that Lamb wave problems in mixed-multilayer regions of non-piezoelectric and piezoelectric materials can be resolved. The field distributions of various Lamb modes in the active regions are then calculated so the mode properties can be studied. The power flows of each of the Lamb modes are calculated using the acoustic Poyntings theorem derived in [53]. This helps determine the amount of energy car-

ried by the modes based on which the strongest modes traveling in the resonators at resonance and antiresonance frequencies are identified.

A design procedure for the frame with a novel working principle is proposed for improving the Q factors of BAW resonators. These high- Q resonators are used to construct the filters operating in the range 2.3–2.4 GHz, which falls within the LTE frequency range. The frame serves as a dual-mode lateral Bragg reflector that is able to reflect the two strongest Lamb modes back into the active region, thereby reducing energy loss due to lateral leakage. The proposed frame, unlike in the case of spurious mode suppression methods, has two raised steps. Each step is designed in such a manner that the step region can be considered as a layer of a lateral Bragg reflector. In order to do that, the characteristic acoustic impedance of each step region is computed for each Lamb mode. A so-called Diffraction Grating Method (DGM) adopted from optics [35], [54] combined with transmission line theory for acoustic guided waves [55] is applied in designing the height and width of the steps. FEM simulation is chosen as a reliable method of verification that is commonly found in literature, e.g. [56], [57] for various types of BAW resonators.

Miniaturization of the designs is also a highly desired feature in modern BAW resonators. Smaller resonators are the key to resolving the overcrowding of physical filters in a smartphone. The effects of a reduced active area on the performance of the BAW resonators is therefore studied. In addition, this work covers the fabrication and characterization of non-framed SMRs with various configurations of their vertical Bragg reflectors. They are designed to reflect dual waves including longitudinal and shear waves in the vertical direction so the acoustic loss in this direction is minimized. The area – performance relation of these fabricated SMRs is also investigated. All the experiments were conducted in the Microsystems and Electronic Materials laboratory of the Technical University of Madrid, Spain.

Chapter 2

Propagation of lateral acoustic waves in BAW resonators

2.1 Lamb waves in an isotropic plate

In an excited infinite solid medium, there are only longitudinal and shear waves traveling in the bulk. The situation, however, differs when the medium is bound by free surfaces, e.g. a thin plate. At the free boundaries of the plate, due to the difference between material properties (of air and plates material), bulk waves undergo such events as reflection, refraction, and mode conversion upon reflection. One example of the mode conversion phenomenon is that when longitudinal waves encounter a free surface, the reflected acoustic energy can trigger particle disturbances in the transverse direction and create shear waves. Here, shear waves refer to the vertical shear (SV) type of waves that are polarized in plane with the longitudinal waves and thus able to interact with them. The horizontal shear (SH) waves, in contrast, are out-of-plane polarized and propagate independently with the other kind of bulk waves. Between two surfaces of the plate, the successively reflected longitudinal and SV waves, when coupling and reconstructing themselves along the plate, generate propagating disturbances named Lamb waves [50]. The plate becomes an acoustic

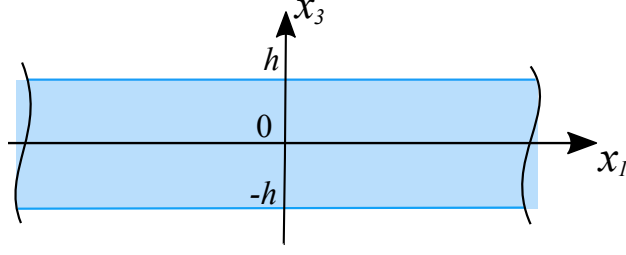


Figure 2.1: An infinite isotropic plate.

waveguide that can support a finite number of propagating and an infinite number of evanescent Lamb modes. These waves are analyzed by solving the guided wave problem, that is, the governed partial differential wave equations with proper physical boundary conditions (BCs). For an isotropic plate (Fig. 2.1), the problem can be formulated as

$$\frac{\partial T_{ij}}{\partial x_j} = \rho \frac{\partial^2 u_i}{\partial t^2} \quad (2.1)$$

$$T_{ij} = c_{ijkl} S_{kl} \quad (2.2)$$

where $i, j, k, l = \overline{1, 3}$. ρ (kg/m³) is the mass density, x_i (m) the Cartesian coordinates, t (s) the time variable, u_i (m) the displacements, T_{ij} (N/m²) the stresses, S_{kl} the strains, and c_{ijkl} (N/m²) the stiffness constants of the material. The plate is a homogeneous medium that has uniform thickness. It is also assumed infinite in the lateral dimensions so the reflection at the side extremities is disregarded. The solutions to (2.1) have to satisfy the BCs: vanishing vertical stress components at free surfaces. This problem can be solved using methods such as FEM, potential theory, or superposition of partial waves. Once solved, the solutions reveal two types of Lamb waves – symmetric modes and antisymmetric modes, depending on the symmetry of their displacement profiles about the median plane. These modes fulfill the Rayleigh–Lamb (R–L) frequency equations, also known as the dispersion relations that non-linearly relate the wavenumber (or in many cases, the wave velocity) to frequency [50, 52, 58]. The relations have the form

$$\frac{\tan(qh)}{\tan(ph)} = -\frac{4k_1^2 pq}{(q^2 - k_1^2)^2} \quad (2.3)$$

for modes that are symmetric about the median plane (denoted as S_i) and

$$\frac{\tan(qh)}{\tan(ph)} = -\frac{(q^2 - k_1^2)^2}{4k_1^2 pq} \quad (2.4)$$

for antisymmetric modes (denoted as A_i).

Here $p^2 = \left(\frac{\omega}{v_L}\right)^2 - k_1^2$ and $q^2 = \left(\frac{\omega}{v_S}\right)^2 - k_1^2$. v_L and v_S (m/s) are, respectively, the velocities of longitudinal and shear waves in the isotropic medium. ω (rad/s) is the angular frequency and k_1 (rad/m) the propagation constant of Lamb modes in the waveguide direction. It is noted that in literature and in the present work, the term wavenumber of Lamb modes, which refers to the inverse wavelength (i.e. $1/\lambda_{\text{Lamb mode}} = k_1/2\pi$ with the unit of $1/m$), is commonly used. There are three cases of k_1 that correspond to various physical meanings. If k_1 is pure real, the waves are propagating waves. If k_1 is positive and pure imaginary, the waves are exponentially decaying waves, assuming that the time harmonic factor has the form $e^{j(k_1 x - \omega t)}$. If k_1 is complex, the waves are oscillatory evanescent waves. These waves play an important role in studying “near field” wave scattering. For a “far field” propagation, the contribution of these waves is often ignored. The R–L equations are transcendental equations and can only be resolved numerically. Fig. 2.2 shows an example of the wave dispersion of a steel plate with $v_L = 5840$ m/s and $v_S = 3150$ m/s plotted only for propagating Lamb modes.

The problem, however, is more complicated for anisotropic media since the crossed terms in (2.1) do not vanish as they do in the isotropic case. Since the method of potentials is no longer applicable in this circumstance, the partial wave technique has to be used instead. At any interface between two media, there are upward and downward bulk waves, denoted by lower indices “ u ” and “ d ” respectively as depicted in Fig. 2.3. In piezoelectric media, apart from quasishear (q–SH and q–SV) and quasilongitudinal (q–L) waves, electromagnetic (EM) waves also propagate in the bulk [59]. Although these partial waves have different wavenumber components k_3 along the x_3 direction, they share the same x_1 component, i.e. k_1 . The solutions

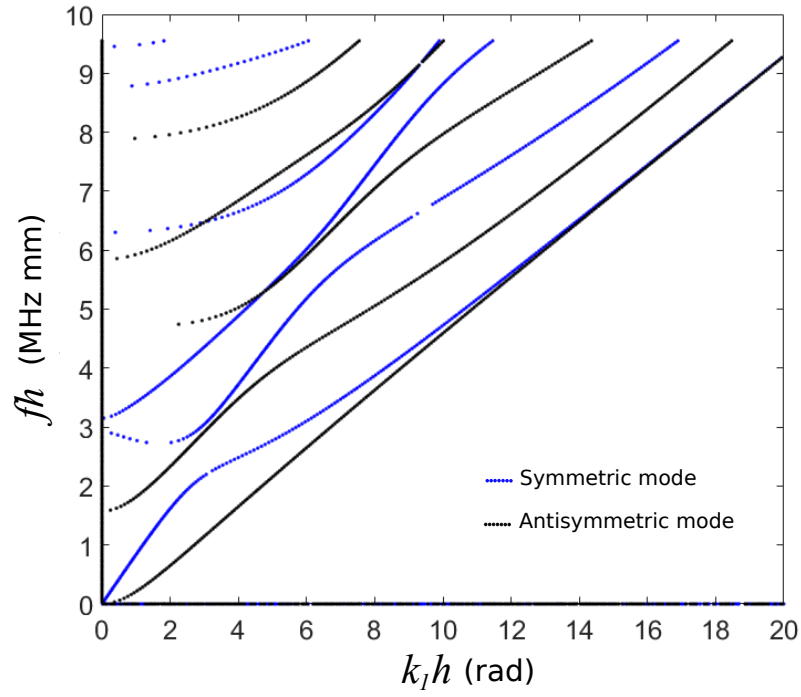


Figure 2.2: Dispersion curves of propagating Lamb modes in an isotropic steel plate where $v_L = 5840$ m/s and $v_S = 3150$ m/s.

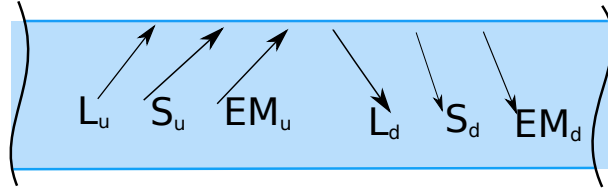


Figure 2.3: Partial waves in a piezoelectric plate.

are the superposition of these waves that satisfy the BCs of the plate. For complex mixed-multilayer structures like the BAW resonators, it is rather difficult to find analytical expressions of Lamb wave solutions. Some attempts are in fact made, but the formulas are restricted to a narrow range of frequencies close to resonance and k_1 range where $k_1 \ll k_3$, with or without the mechanical contribution of the electrodes to the acoustic behavior of Lamb modes [60], [61]. Traditionally, due to the complexity of the problem, a numerical search is necessary and is associated with matrix techniques, e.g. Transfer Matrix or Global Matrix method, to find the wave solutions for large frequency and k_1 ranges. These techniques are semi-analytical methods and need to be aided by powerful computational systems.

2.2 Transfer matrix (TM) method

The TM method, first introduced by Thomson [62] and Haskell [63] for directly solving the wave problem in stratified media, can also be found in many other studies. The aim is to analyze the waves in various media and layered structures, for instance, solving a 2D problem in a stack of all isotropic layers [64], in a single piezoelectric layer [65], [66], in non-piezoelectric monoclinic multilayered media [67], in piezoelectric multilayers [68], or in a 1D problem of piezoelectric resonators [69–71]. For guided wave problems in multilayers, the TM relates the electrical and mechanical fields at the lower surface to those at the upper surface. The fields at the intermediate interfaces are eliminated due to continuity properties and substitutions.

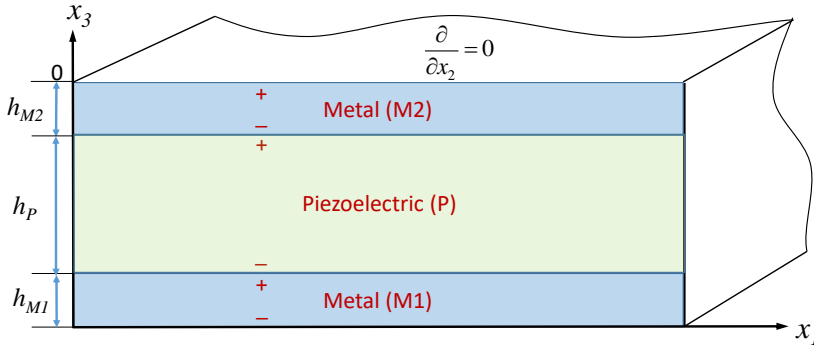


Figure 2.4: Simplified FBAR schematic for guided Lamb wave analysis.

In the present work, the TM method is applied to the mixed-multilayer BAW resonators to find the solutions for guided Lamb waves along the active region (2D problem). The structure to be analyzed is depicted in Fig. 2.4. The perfectly conducting electrodes with isotropic property are treated as layers with fully defined mechanical and electrical properties. The problem is, in the electrode layers, the vanishing of EM partial waves causes the size of their layer matrices to shrink. Indeed, there are only six partial waves (upward and downward longitudinal, SV, SH waves) in isotropic media, as opposed to eight partial waves (upward and downward q-L, q-SV, q-SH, EM waves) in piezoelectric media. This leads to a failure in

the interfacial matrix multiplications between the piezoelectric layer and the electrodes. Therefore, the expressions for electrical fields must be included in the matrix representation of the electrodes.

For piezoelectric media, the constitutive equations must also be satisfied

$$T_{ij} = c_{ijkl}^E S_{kl} - e_{kij} E_k \quad , \quad (2.5)$$

$$D_i = e_{ijk} S_{jk} + \varepsilon_{ij}^S E_j \quad , \quad (2.6)$$

where $S_{kl} = \frac{1}{2} \left(\frac{\partial u_k}{\partial x_l} + \frac{\partial u_l}{\partial x_k} \right)$ and $E_k = -\frac{\partial \phi}{\partial x_k}$. e_{kij} (C/m²), ε_{ij} (F/m), E_k (V/m), D_i (C/m²), and ϕ (V) are, respectively, the piezoelectric constants, dielectric constants, electrical field, electrical displacement field, and potential. Here, the superscripts E and S above c_{ijkl} and ε_{ij} indicate that these parameters are measured under constant \mathbf{E} and \mathbf{S} fields. Equation (2.1) thus becomes

$$c_{ijkl} \frac{\partial^2 u_k}{\partial x_j \partial x_l} + e_{kij} \frac{\partial^2 \phi}{\partial x_j \partial x_k} = \rho \frac{\partial^2 u_i}{\partial t^2} \quad (2.7)$$

Assume that the particle displacements and the potential of the partial waves have time-dependent harmonic forms

$$u_i^{par} = A_i e^{jk_3 x_3} e^{j(k_1 x_1 - \omega t)} \quad , \quad i = \overline{1, 3} \quad (2.8)$$

$$\phi^{par} = A_4 e^{jk_3 x_3} e^{j(k_1 x_1 - \omega t)} \quad (2.9)$$

and plane strain, i.e. $\partial/\partial x_2$ vanishes, (2.7) can be written, e.g. for u_1^{par} , as

$$\begin{aligned} & c_{1111} \frac{\partial^2 u_1^{par}}{\partial x_1^2} + c_{1113} \frac{\partial^2 u_1^{par}}{\partial x_1 \partial x_3} + c_{1311} \frac{\partial^2 u_1^{par}}{\partial x_3 \partial x_1} + c_{1313} \frac{\partial^2 u_1^{par}}{\partial x_3^2} + c_{1121} \frac{\partial^2 u_2^{par}}{\partial x_1^2} + c_{1123} \frac{\partial^2 u_2^{par}}{\partial x_1 \partial x_3} + \\ & + c_{1321} \frac{\partial^2 u_2^{par}}{\partial x_3 \partial x_1} + c_{1323} \frac{\partial^2 u_2^{par}}{\partial x_3^2} + c_{1131} \frac{\partial^2 u_3^{par}}{\partial x_1^2} + c_{1133} \frac{\partial^2 u_3^{par}}{\partial x_1 \partial x_3} + c_{1331} \frac{\partial^2 u_3^{par}}{\partial x_3 \partial x_1} + c_{1333} \frac{\partial^2 u_3^{par}}{\partial x_3^2} + \\ & + e_{111} \frac{\partial^2 \phi^{par}}{\partial x_1^2} + e_{311} \frac{\partial^2 \phi^{par}}{\partial x_3 \partial x_1} + e_{113} \frac{\partial^2 \phi^{par}}{\partial x_1 \partial x_3} + e_{313} \frac{\partial^2 \phi^{par}}{\partial x_3^2} = \rho \frac{\partial^2 u_1^{par}}{\partial t^2} \quad . \end{aligned} \quad (2.10)$$

The same derivations can be made for u_2 and u_3 . The electrical displacement field

also satisfies the electrostatic approximation

$$\nabla \cdot \mathbf{D} = 0 \quad (2.11)$$

which can be expanded as

$$\begin{aligned} & e_{111} \frac{\partial^2 u_1^{par}}{\partial x_1^2} + e_{113} \frac{\partial^2 u_1^{par}}{\partial x_1 \partial x_3} + e_{311} \frac{\partial^2 u_1^{par}}{\partial x_3 \partial x_1} + e_{313} \frac{\partial^2 u_1^{par}}{\partial x_3^2} + e_{121} \frac{\partial^2 u_2^{par}}{\partial x_1^2} + e_{123} \frac{\partial^2 u_2^{par}}{\partial x_1 \partial x_3} + \\ & + e_{321} \frac{\partial^2 u_2^{par}}{\partial x_3 \partial x_1} + e_{323} \frac{\partial^2 u_2^{par}}{\partial x_3^2} + e_{131} \frac{\partial^2 u_3^{par}}{\partial x_1^2} + e_{133} \frac{\partial^2 u_3^{par}}{\partial x_1 \partial x_3} + e_{331} \frac{\partial^2 u_3^{par}}{\partial x_3 \partial x_1} + e_{333} \frac{\partial^2 u_3^{par}}{\partial x_3^2} - \\ & - \varepsilon_{11} \frac{\partial^2 \phi^{par}}{\partial x_1^2} - \varepsilon_{31} \frac{\partial^2 \phi^{par}}{\partial x_3 \partial x_1} - \varepsilon_{13} \frac{\partial^2 \phi^{par}}{\partial x_1 \partial x_3} - \varepsilon_{33} \frac{\partial^2 \phi^{par}}{\partial x_3^2} = 0 \quad . \end{aligned} \quad (2.12)$$

The second order partial differentiations of the various fields in (2.10) and (2.12) are

$$\begin{aligned} \frac{\partial^2 u_i^{par}}{\partial x_1^2} &= -k_1^2 u_i^{par} \quad ; \quad \frac{\partial^2 u_i^{par}}{\partial x_3^2} = -k_3^2 u_i^{par} \quad ; \quad \frac{\partial^2 u_i^{par}}{\partial x_1 \partial x_3} = -k_1 k_3 u_i^{par} \quad ; \quad \frac{\partial^2 u_i^{par}}{\partial t^2} = -\omega^2 u_i^{par} \quad ; \\ \frac{\partial^2 \phi^{par}}{\partial x_1^2} &= -k_1^2 \phi^{par} \quad ; \quad \frac{\partial^2 \phi^{par}}{\partial x_3^2} = -k_3^2 \phi^{par} \quad ; \quad \frac{\partial^2 \phi^{par}}{\partial x_1 \partial x_3} = -k_1 k_3 \phi^{par} \quad . \end{aligned} \quad (2.13)$$

Together (2.7)–(2.9), (2.12), and (2.13) form the Christoffel equation

$$\underbrace{\begin{bmatrix} \Gamma_{11} - \rho\omega^2 & \Gamma_{12} & \Gamma_{13} & \Gamma_{14} \\ \Gamma_{21} & \Gamma_{22} - \rho\omega^2 & \Gamma_{23} & \Gamma_{24} \\ \Gamma_{31} & \Gamma_{32} & \Gamma_{33} - \rho\omega^2 & \Gamma_{34} \\ \Gamma_{41} & \Gamma_{42} & \Gamma_{43} & \Gamma_{44} \end{bmatrix}}_{\mathbf{\Gamma}} \cdot \underbrace{\begin{bmatrix} A_1 \\ A_2 \\ A_3 \\ A_4 \end{bmatrix}}_{\mathbf{A}} = \mathbf{\Gamma A} = \mathbf{0} \quad (2.14)$$

where

$$\begin{aligned} \Gamma_{ij} &= c_{3i3j} k_3^2 + (c_{3i1j} + c_{1i3j}) k_1 k_3 + c_{1i1j} k_1^2 \quad , \quad i, j = \overline{1, 3} \quad , \\ \Gamma_{i4} &= \Gamma_{4i} = e_{3i3} k_3^2 + (e_{1i3} + e_{3i1}) k_1 k_3 + e_{1i1} k_1^2 \quad , \\ \Gamma_{44} &= -[\varepsilon_{33} k_3^2 + (\varepsilon_{13} + \varepsilon_{31}) k_1 k_3 + \varepsilon_{11} k_1^2] \quad . \end{aligned} \quad (2.15)$$

and $A_n, n = \overline{1, 4}$ are the coefficients of polarization of the partial waves. The linear

system of equations in (2.14) has non-trivial solutions when

$$|\mathbf{\Gamma}| = 0 \quad . \quad (2.16)$$

Equation (2.16) is an eight-order polynomial equation whose eight roots are the propagation constants of eight partial waves. Each root corresponds to a polarization vector \mathbf{A} , thus there are a total of eight four-component polarization vectors denoted by A_{rp} ($r = \overline{1,4}$ and $p = \overline{1,8}$). The solutions to (2.7) are, as mentioned, the superposition of all the found partial waves

$$u_i^{Lamb} = e^{j(k_1 x_1 - \omega t)} \sum_{p=1}^8 A_{ip} C_p e^{j k_3^{(p)} x_3} \quad , \quad (2.17)$$

$$\phi^{Lamb} = e^{j(k_1 x_1 - \omega t)} \sum_{p=1}^8 A_{4p} C_p e^{j k_3^{(p)} x_3} \quad , \quad (2.18)$$

where C_p are the coefficients of the eight partial waves. The expressions for normal stress components and electrical displacement are obtained by substituting (2.17) and (2.18) into (2.5) and (2.6), respectively. In order to implement the TM technique, a state vector $\mathbf{P}_{\text{state}}$ comprising u_i^{Lamb} , T_{3i}^{Lamb} , D_3^{Lamb} , and ϕ^{Lamb} components is defined. More specifically, $\mathbf{P}_{\text{state}}$ can be expressed as

$$\begin{aligned} \mathbf{P}_{\text{state}} = \begin{bmatrix} u_1^{Lamb} \\ u_2^{Lamb} \\ u_3^{Lamb} \\ D_3^{Lamb} \\ T_{31}^{Lamb} \\ T_{32}^{Lamb} \\ T_{33}^{Lamb} \\ \phi^{Lamb} \end{bmatrix} &= \underbrace{\begin{bmatrix} A_{11} & A_{12} & A_{13} & A_{14} & A_{15} & A_{16} & A_{17} & A_{18} \\ A_{21} & A_{22} & A_{23} & A_{24} & A_{25} & A_{26} & A_{27} & A_{28} \\ A_{31} & A_{32} & A_{33} & A_{34} & A_{35} & A_{36} & A_{37} & A_{38} \\ G_{31} & G_{32} & G_{33} & G_{34} & G_{35} & G_{36} & G_{37} & G_{38} \\ F_{11} & F_{12} & F_{13} & F_{14} & F_{15} & F_{16} & F_{17} & F_{18} \\ F_{21} & F_{22} & F_{23} & F_{24} & F_{25} & F_{26} & F_{27} & F_{28} \\ F_{31} & F_{32} & F_{33} & F_{34} & F_{35} & F_{36} & F_{37} & F_{38} \\ A_{41} & A_{42} & A_{43} & A_{44} & A_{45} & A_{46} & A_{47} & A_{48} \end{bmatrix}}_{\mathbf{X}} \mathbf{W} \mathbf{C} e^{j(k_1 x_1 - \omega t)} \\ &= \mathbf{X} \mathbf{W} \mathbf{C} e^{j(k_1 x_1 - \omega t)} \end{aligned} \quad (2.19)$$

where \mathbf{W} is the diagonal matrix whose entries have the form $e^{jk_3^{(p)}x_3}$ and \mathbf{C} is the vector of coefficients. \mathbf{X} is called state matrix. The term $e^{j(k_1x_1-\omega t)}$ is the common term in the BC equations and can be omitted when the matrices are computed. In (2.19),

$$G_{3p} = jk_1\epsilon_{3q1} \sum_{p=1}^8 A_{qp} + je_{3q3} \sum_{p=1}^8 k_3^{(p)} A_{qp} - jk_1\epsilon_{31} \sum_{p=1}^8 A_{4p} - j\epsilon_{33} \sum_{p=1}^8 k_3^{(p)} A_{4p} \quad , \quad q = \overline{1,3} \quad (2.20)$$

and

$$F_{mp} = jk_1c_{3m1n} \sum_{p=1}^8 A_{np} + jc_{3m3n} \sum_{p=1}^8 k_3^{(p)} A_{np} + jk_1e_{13m} \sum_{p=1}^8 A_{4p} + je_{33m} \sum_{p=1}^8 k_3^{(p)} A_{4p} \quad , \quad m, n = \overline{1,3} \quad (2.21)$$

The 8×8 layer transfer matrix \mathbf{L}_{Piezo} of the piezoelectric layer is constructed as presented in *Paper 3* so that

$$\mathbf{P}_{\text{state,Piezo}}^+ = \mathbf{L}_{\text{Piezo}} \mathbf{P}_{\text{state,Piezo}}^- \quad , \quad (2.22)$$

Here, the upper notations $^+$ and $^-$ denote the upper and lower surfaces of a layer. For the metal electrodes, which are isotropic and perfectly conductive, the coupling constants e in (2.5) and (2.6) are zero and each electrode layer is equipotential. Under these conditions, (2.5) reduces to (2.2) and the EM partial waves in these layers vanish. The Christoffel matrix $\mathbf{\Gamma}$, consequently, reduces to a 3×3 matrix according to which equation (2.16) has only six roots. As a result, the layer transfer matrices $\mathbf{L}_{\mathbf{M1}}$ and $\mathbf{L}_{\mathbf{M2}}$ of the bottom and top electrodes reduce to 6×6 matrices. The overall transfer matrix of the resonator is the product of $\mathbf{L}_{\mathbf{M2}}$, $\mathbf{L}_{\text{Piezo}}$, and $\mathbf{L}_{\mathbf{M1}}$. Therefore, $\mathbf{L}_{\mathbf{M1}}$ and $\mathbf{L}_{\mathbf{M2}}$ have to be modified by introducing the electrical relations between the lower and upper surfaces of each electrode layer so they become 8×8 matrices. That is, for the top electrode,

$$D_{3,M2}^+ = \frac{jY}{\omega A} \phi + D_{3,M2}^- \quad (2.23)$$

$$\phi_{M2}^+ = \phi_{M2}^- \quad (2.24)$$

where Y is the electrical admittance of the resonator and A the overlapped area between the electrodes. A similar expression can be written for the bottom electrode, only that the current has an opposite sign. The wave problem is subsequently simplified as

$$\mathbf{P}_{\text{state}, \mathbf{M}2}^+ = \mathbf{L} \mathbf{P}_{\text{state}, \mathbf{M}1}^- \quad (2.25)$$

Here \mathbf{L} is the overall transfer matrix. The BC applied to (2.25) includes

- mechanical BCs, free traction on free surfaces;
- electrical BCs, either zero potentials (short circuit condition, $1/Y \rightarrow 0$) or zero D_3 (open circuit condition, $Y \rightarrow 0$) on free surfaces.

Solving these BC equations results in the dispersion diagram of the analyzed structure. The advantage of this technique is that the matrices to be handled are relatively small in dimension (8×8), compared with the Global Matrix method introduced in the following section. The numerical error caused by large matrices is thus reduced and common zero finding algorithms like bisection or Newton's method can be applied. However, due to the large difference between, e.g. the entries of \mathbf{X} matrix in (2.19), the transfer matrices could be badly scaled. To avoid this type of numerical error, it is essential to non-dimensionalize the quantities. Therefore

$$\begin{aligned} k'_1 &= \frac{h_{Piezo}}{2\pi} k_1 \quad , \quad k'_3 = \frac{h_{Piezo}}{2\pi} k_3 \quad , \quad c'_{ijkl} = \frac{c_{ijkl}}{c_{3131, Piezo}} \quad , \\ e'_{kij} &= \frac{e_{kij}}{\sqrt{c_{3131, Piezo} \varepsilon_{33}}} \quad , \quad \varepsilon'_{ij} = \frac{\varepsilon_{ij}}{\varepsilon_{33}} \quad , \quad \omega' = \frac{h_{Piezo}}{2\pi} \frac{\omega}{\sqrt{c_{3131, Piezo}}} \end{aligned} \quad (2.26)$$

are used in the equations instead of $k_1, k_3, c_{ijkl}, e_{kij}, \varepsilon_{ij}$, and ω respectively. The disadvantage of the TM method is that, due to the matrix manipulation of the electrode layers, it is difficult to find \mathbf{C} through matrix inversion in order to compute all the fields in the analyzed structure.

2.3 Global Matrix method

The Global Matrix (GM) technique is also a common method for solving wave problems in stratified structures. It was first developed by Knopoff [72] and can also be found in later work [73–78]. Unlike the TM method, in the GM method all the BCs at the layer interfaces and surfaces are assembled together, including

- The continuity of mechanical (normal stress T_{3i}^{Lamb} and displacement components) and electrical fields at each interface between two layers;
- The vanishing of T_{3i}^{Lamb} on the upper and lower surfaces;
- Either short circuit or open circuit condition on the two free surfaces. (2.27)

As a result, when the number of layers increases, the number of BCs increases and so does the size of the GM. For each layer in the stratified structure shown in Fig. 2.4, defining

$$\mathbf{N} = \mathbf{X}\mathbf{W} \quad , \quad (2.28)$$

the GM can be written as

$$\underbrace{\begin{bmatrix} -\mathbf{N}^{3+} & \mathbf{0} & \mathbf{0} \\ \mathbf{N}^{3-} & -\mathbf{N}^{2+} & \mathbf{0} \\ \mathbf{0} & \mathbf{N}^{2-} & -\mathbf{N}^{1+} \\ \mathbf{0} & \mathbf{0} & \mathbf{N}^{1-} \end{bmatrix}}_{\mathbf{Z}} \underbrace{\begin{bmatrix} \mathbf{C}_3 \\ \mathbf{C}_2 \\ \mathbf{C}_1 \end{bmatrix}}_{\mathbf{C}} = \mathbf{Z}\mathbf{C} = \mathbf{0} \quad (2.29)$$

Here \mathbf{Z} is the global matrix, the upper notations i^+ and i^- denote the upper and lower interfaces of the i^{th} layer. $i=1, 2, 3$ for the M1, piezoelectric, and M2 layers, respectively. It is noted that the stack is bounded by vacuum (or air) in which all the fields vanish, subsequently $\mathbf{N}^{4-} = \mathbf{N}^{0+} = \mathbf{0}$ and the field continuity conditions are replaced by the BCs on free surfaces. Hence \mathbf{Z} can be expanded, e.g. for the open circuit BC described in (2.27), as expressed in (2.30). Equation (2.30) has

non-trivial solutions when the GM matrix \mathbf{Z} is singular, i.e. the matrix has zero determinant. However, for the GM method, even when non-dimensionalizations are carried out, using zero determinant as a criterion for judging the singularity of the matrix is not recommended due to large numerical error. A criterion for condition number – the ratio between the largest and smallest non-negative singular values – is thus used to solve (2.29) instead. These singular values are found by taking the singular value decomposition (SVD) of \mathbf{Z} [79]. More information about this mathematical technique is provided in *Paper 3*. Although the GM size is generally larger than that of the TM (e.g. a 22×22 matrix found in eq. (2.30) versus an 8×8 \mathbf{L} matrix for the same three-mixed-layer stack), by using the GM method all the fields (\mathbf{u}^{Lamb} , \mathbf{T}^{Lamb} , \mathbf{D}^{Lamb} , \mathbf{E}^{Lamb}) at any position in the resonator can be readily reconstructed once \mathbf{C} is obtained from the SVD. This method is thus more preferable for any further analyses that require these fields such as for calculating the complex acoustic Poynting vector.

$$\begin{array}{c}
 D_3 \\
 T_{31} \\
 T_{32} \\
 T_{33} \\
 u_1 \\
 u_2 \\
 u_3 \\
 D_3 \\
 T_{31} \\
 T_{32} \\
 T_{33} \\
 u_1 \\
 u_2 \\
 u_3 \\
 D_3 \\
 T_{31} \\
 T_{32} \\
 T_{33} \\
 D_3 \\
 T_{31} \\
 T_{32} \\
 T_{33}
 \end{array}
 \begin{array}{c}
 \left[\begin{array}{cccccc|c}
 0 & 0 & 0 & 0 & 0 & 0 & -1 \\
 -N_{51}^{3+} & -N_{52}^{3+} & -N_{53}^{3+} & -N_{54}^{3+} & -N_{55}^{3+} & -N_{56}^{3+} & 0 \\
 -N_{61}^{3+} & -N_{62}^{3+} & -N_{63}^{3+} & -N_{64}^{3+} & -N_{65}^{3+} & -N_{66}^{3+} & 0 \\
 -N_{71}^{3+} & -N_{72}^{3+} & -N_{73}^{3+} & -N_{74}^{3+} & -N_{75}^{3+} & -N_{76}^{3+} & 0
 \end{array} \right] \\
 \left[\begin{array}{cccccc|c}
 N_{11}^{2+} & N_{12}^{2+} & N_{13}^{2+} & N_{14}^{2+} & N_{15}^{2+} & N_{16}^{2+} & 0 \\
 N_{21}^{2+} & N_{22}^{2+} & N_{23}^{2+} & N_{24}^{2+} & N_{25}^{2+} & N_{26}^{2+} & 0 \\
 N_{31}^{2+} & N_{32}^{2+} & N_{33}^{2+} & N_{34}^{2+} & N_{35}^{2+} & N_{36}^{2+} & 0 \\
 0 & 0 & 0 & 0 & 0 & 0 & 1 \\
 N_{51}^{2+} & N_{52}^{2+} & N_{53}^{2+} & N_{54}^{2+} & N_{55}^{2+} & N_{56}^{2+} & 0 \\
 N_{61}^{2+} & N_{62}^{2+} & N_{63}^{2+} & N_{64}^{2+} & N_{65}^{2+} & N_{66}^{2+} & 0 \\
 N_{71}^{2+} & N_{72}^{2+} & N_{73}^{2+} & N_{74}^{2+} & N_{75}^{2+} & N_{76}^{2+} & 0
 \end{array} \right] \\
 \left[\begin{array}{cccccc|c}
 N_{11}^{2-} & N_{12}^{2-} & N_{13}^{2-} & N_{14}^{2-} & N_{15}^{2-} & N_{16}^{2-} & 0 \\
 N_{21}^{2-} & N_{22}^{2-} & N_{23}^{2-} & N_{24}^{2-} & N_{25}^{2-} & N_{26}^{2-} & 0 \\
 N_{31}^{2-} & N_{32}^{2-} & N_{33}^{2-} & N_{34}^{2-} & N_{35}^{2-} & N_{36}^{2-} & 0 \\
 N_{41}^{2-} & N_{42}^{2-} & N_{43}^{2-} & N_{44}^{2-} & N_{45}^{2-} & N_{46}^{2-} & 0 \\
 N_{51}^{2-} & N_{52}^{2-} & N_{53}^{2-} & N_{54}^{2-} & N_{55}^{2-} & N_{56}^{2-} & 0 \\
 N_{61}^{2-} & N_{62}^{2-} & N_{63}^{2-} & N_{64}^{2-} & N_{65}^{2-} & N_{66}^{2-} & 0 \\
 N_{71}^{2-} & N_{72}^{2-} & N_{73}^{2-} & N_{74}^{2-} & N_{75}^{2-} & N_{76}^{2-} & 0
 \end{array} \right] \\
 \left[\begin{array}{cccccc|c}
 N_{11}^{1+} & N_{12}^{1+} & N_{13}^{1+} & N_{14}^{1+} & N_{15}^{1+} & N_{16}^{1+} & 0 \\
 N_{21}^{1+} & N_{22}^{1+} & N_{23}^{1+} & N_{24}^{1+} & N_{25}^{1+} & N_{26}^{1+} & 0 \\
 N_{31}^{1+} & N_{32}^{1+} & N_{33}^{1+} & N_{34}^{1+} & N_{35}^{1+} & N_{36}^{1+} & 0 \\
 0 & 0 & 0 & 0 & 0 & 0 & -1 \\
 N_{51}^{1+} & N_{52}^{1+} & N_{53}^{1+} & N_{54}^{1+} & N_{55}^{1+} & N_{56}^{1+} & 0 \\
 N_{61}^{1+} & N_{62}^{1+} & N_{63}^{1+} & N_{64}^{1+} & N_{65}^{1+} & N_{66}^{1+} & 0 \\
 N_{71}^{1+} & N_{72}^{1+} & N_{73}^{1+} & N_{74}^{1+} & N_{75}^{1+} & N_{76}^{1+} & 0
 \end{array} \right] \\
 \left[\begin{array}{cccccc|c}
 0 & 0 & 0 & 0 & 0 & 0 & 1 \\
 N_{51}^{1-} & N_{52}^{1-} & N_{53}^{1-} & N_{54}^{1-} & N_{55}^{1-} & N_{56}^{1-} & 0 \\
 N_{61}^{1-} & N_{62}^{1-} & N_{63}^{1-} & N_{64}^{1-} & N_{65}^{1-} & N_{66}^{1-} & 0 \\
 N_{71}^{1-} & N_{72}^{1-} & N_{73}^{1-} & N_{74}^{1-} & N_{75}^{1-} & N_{76}^{1-} & 0
 \end{array} \right]
 \end{array}
 \begin{array}{c}
 C_{31} \\
 C_{32} \\
 C_{33} \\
 C_{34} \\
 C_{35} \\
 C_{36} \\
 C_{37} \\
 C_{21} \\
 C_{22} \\
 C_{23} \\
 C_{24} \\
 C_{25} \\
 C_{26} \\
 C_{27} \\
 C_{28} \\
 C_{11} \\
 C_{12} \\
 C_{13} \\
 C_{14} \\
 C_{15} \\
 C_{16} \\
 C_{17}
 \end{array}
 = \mathbf{0}
 \quad (2.30)$$

2.4 Testing the methods

The analyzed structure is a simplified FBAR model comprising a stack of three layers – two tungsten (W) layers, each one of 115 nm thick, serving as the metal electrodes, and an AlN layer 1150 nm thick, serving as the piezoelectric layer. The structure is thus symmetric about the median plane. In the TM method, the local coordinate system is used for each layer in order to simplify the calculations. In the GM method, a global coordinate system in which the origin is placed at the middle of the AlN layer, is used instead. In this way, the reconstructed fields are either symmetric or antisymmetric about the median plane and various Lamb modes can be identified easier. It is noted that solving (2.7) not only gives Lamb wave solutions but also the solutions for the out-of-plane SH waves which independently propagate in the plate. In the present work, in order to reduce the size of the matrices, these out-of-plane SH waves are initially excluded by omitting the u_2^{Lamb} and T_{32}^{Lamb} terms in all equations.

The vertically propagating waves in the piezoelectric layer of a BAW resonator are rather q-L and q-S waves than “pure” longitudinal and shear waves. The main operating mode in the analyzed resonator is the fundamental q-L mode, or first-order thickness extensional TE_1 mode. The frequency at which this mode resonates depends on the lateral dimensions of the resonator. A detailed explanation for this property is given in Chapter 4. At the moment, to achieve a good agreement among the results of FEM simulation and the two matrix techniques in which the analyzed stack is assumed laterally infinite, the length of the simulated FBAR needs to be sufficiently large. Here it is chosen to be 200 μm .

Fig. 2.5 and Fig. 2.6 show the dispersion diagram of the FBAR computed from various methods including TM, GM, and FEM. The FEM results are obtained by taking the discrete Fourier transform (DFT) of the extracted vertical displacement on the top surface of the FBAR’s active region [57], [80], [81]. From Fig. 2.5 and Fig. 2.6, it can be observed that the electrical BC at the free surfaces strongly affects the S_i

modes but not the A_i modes at frequencies around f_r and f_a . The mode shapes of these Lamb modes can help to explain the phenomenon. For the A_i modes, also called flexural modes, the periodic flexing motions of the horizontal boundaries does not change the relative spacing between them. The mode-induced voltage across the two electrodes at any point on the resonator thus remains constant. In other words, these A_i modes cannot be directly excited or affected by the constant applied electrical field over the electrode surfaces. Dilatational S_i modes, in contrast, do not have such a behavior due to their symmetric profiles of contraction and expansion regions of the resonator about its median plane. The voltage induced by these modes are different at different points on the resonator. The applied field thus has a significant impact on them, especially at the frequency range where the electromechanical coupling is the largest. In the short circuit case, the cut-off frequency of the S_1 mode coincides with the resonance frequency of the TE_1 mode. In fact, at resonance frequency, the electrical admittance Y is at maximum (tends to infinite), similar to what happens in the short circuit condition. The cut-off frequency of S_1 , on the other hand, occurs at antiresonance frequency of the TE_1 mode in the open circuit case, where electrical admittance is at minimum (tends to zero). For type-II resonators, the S_1 mode dispersion curve has two branches – to the left of the mode's bifurcated point the curve's slope is negative (hence named S_{1-}) and vice versa for the one to the right of that point (thus called S_{1+}).

In the GM method, in addition to the Lamb wave solutions, there are other solutions represented by the (dotted) straight lines as seen in Fig. 2.5 and Fig. 2.6. The reason is that the GM takes into account all the bulk waves in the internal layers. If the wavenumber of the solution Lamb wave is approximately that of the bulk wave, then the GM is also singular due to identical columns. Indeed, the wave velocity calculated from the line with the smallest slope is 2880 m/s, which is the velocity of shear wave in tungsten. For the line with the largest slope, the wave velocity is 10290 m/s, which is approximately the velocity of q-L waves in AlN. However, since they are the bulk waves in each internal layer, they cannot satisfy the conditions of

field continuity across the layer interfaces and thus can be distinguished from the Lamb waves.

The displacement profiles of various Lamb modes plotted in Fig. 2.7 and Fig. 2.8 show the notable symmetry of these modes. That is, symmetric Lamb modes have symmetric u_1 and antisymmetric u_3 about the median plane whereas antisymmetric Lamb modes have antisymmetric u_1 and symmetric u_3 about this plane. This agrees with the symmetry properties of propagating Lamb modes in a single-layered isotropic plate [52]. However, when the thickness of the top tungsten electrode is gradually increased, the structure loses its symmetry and so does the mode shape. The modes behave like the so-called generalized Lamb waves as mentioned in references [50], [82]. Fig. 2.9 shows the phase velocity of guided waves in a W/AlN/W stack in which the thickness of the top tungsten layer is ten times larger than the one in Fig. 2.5. Here the modes, despite their antisymmetric profiles, are still named as A_i and S_i modes, analogous to those found in the 115 nm/1150 nm/115 nm case. This analogy shall serve the frame design method presented in the following chapter. For a large thickness of the top tungsten layer and a high frequency, the low order mode (A_0 and S_0) velocities approach the velocity of Rayleigh waves traveling in

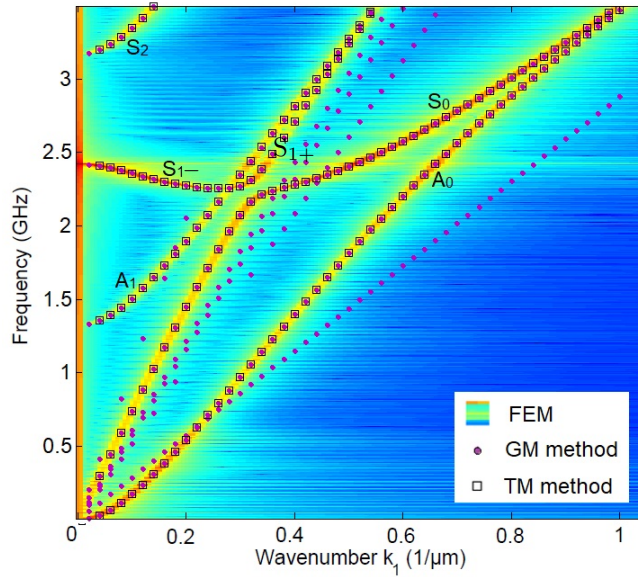


Figure 2.5: Dispersion curves of an FBAR's active region by various methods. The stack configuration is W/AlN/W of 115 nm/1150 nm/115 nm thick. The short circuit boundary condition is used on the free surfaces of the stack.

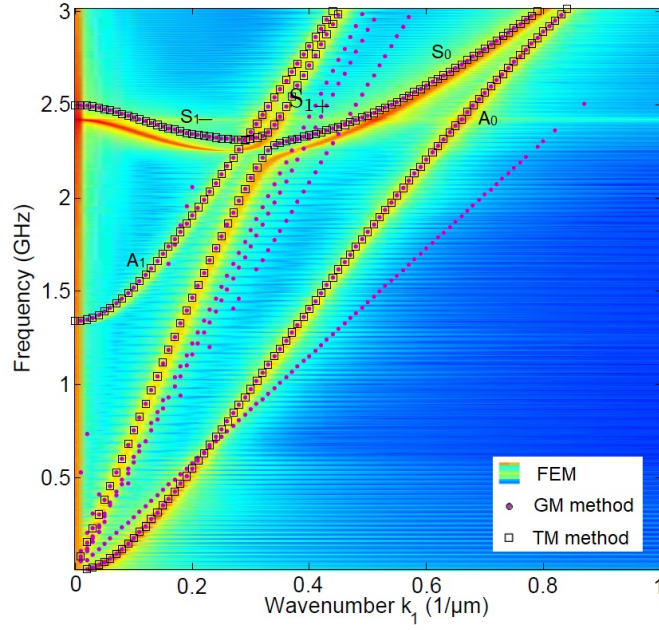


Figure 2.6: Dispersion curves of an FBAR's active region by various methods. The stack configuration is W/AlN/W of 115 nm/1150 nm/115 nm thick. The open circuit boundary condition is used on the free surfaces of the stack but only for the matrix methods.

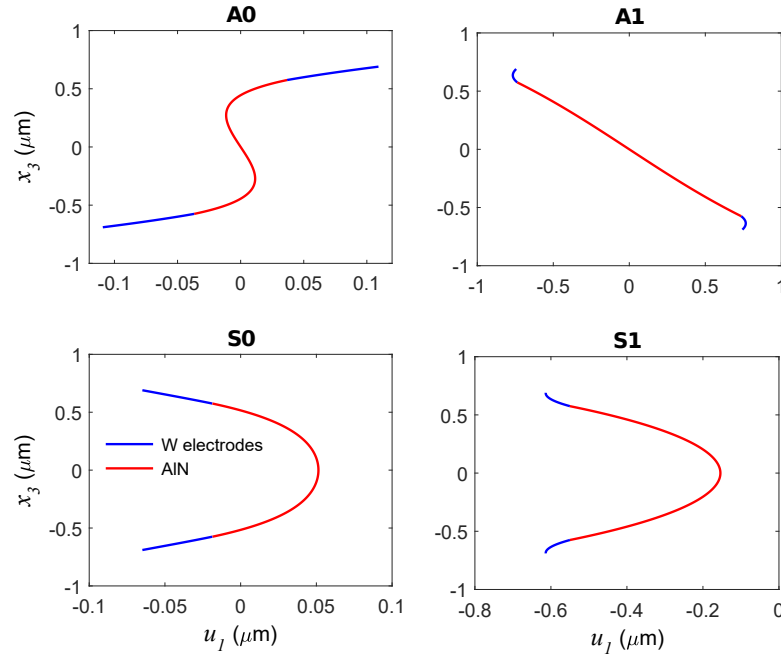


Figure 2.7: Displacement profiles u_1 of various Lamb modes propagating in a W/AlN/W stack of 115 nm/1150 nm/115 nm thick at antiresonance frequency.

tungsten, which is given in [83].

$$V_R \approx \frac{0.874 + 1.2\nu}{1 + \nu} v_S = 2672 \text{ (m/s)}. \quad (2.31)$$

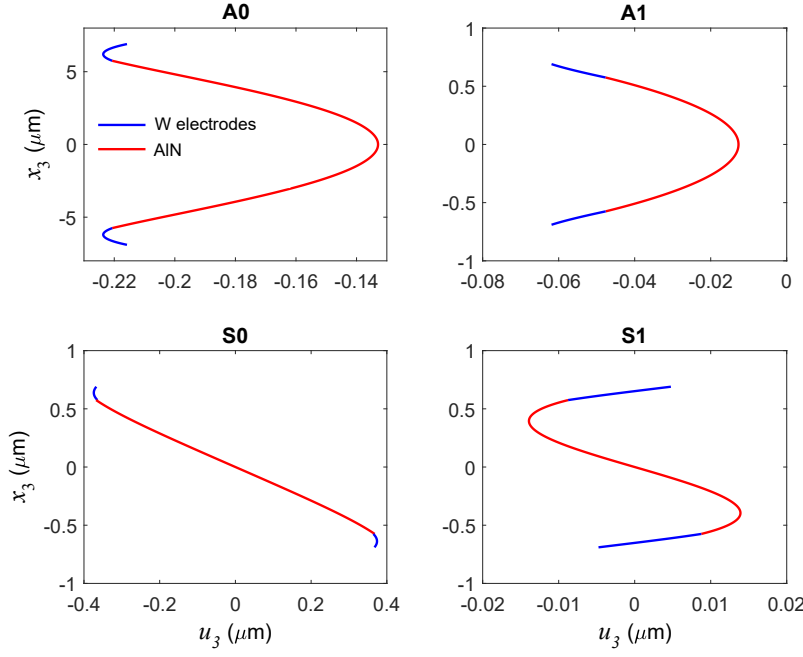


Figure 2.8: Displacement profiles u_3 of various Lamb modes propagating in a W/AlN/W stack of 115 nm/1150 nm/115 nm thick at antiresonance frequency.

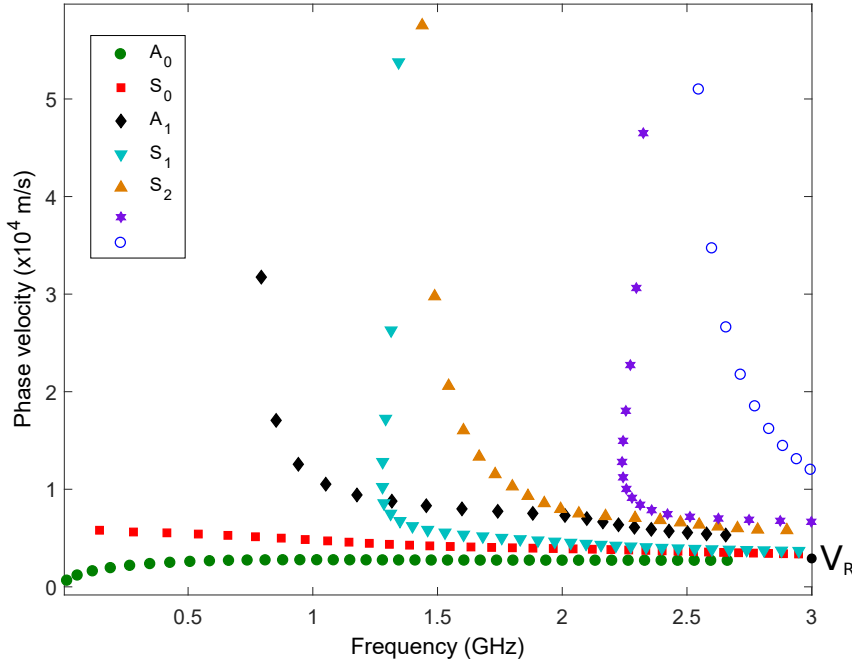


Figure 2.9: Dispersion diagram of guided waves in a W/AlN/W stack in which the thickness ratio between the layers is 1150 nm/1150 nm/115 nm. V_R is the velocity of Rayleigh waves in tungsten.

Here, $\nu=0.28$ and $v_s=2880$ m/s are the Poissons ratio and velocity of shear waves in tungsten, respectively. At a relatively high frequency, e.g. 3 GHz, the wavelength

of a Rayleigh wave is

$$\lambda_R = \frac{V_R}{3 \times 10^9 \text{ Hz}} \approx 891 \text{ (nm)}. \quad (2.32)$$

The top tungsten layer thickness is comparable with this λ_R and under this condition, the A_0 and S_0 Lamb modes become surface acoustic waves of Rayleigh type that propagate on the surface of the top tungsten layer. If the height of the top tungsten step is further increased, this phenomenon starts to occur at an even lower frequency. The velocities of the A_1 , S_1 , and higher order modes, on the other hand, approach the velocity of shear waves in tungsten when the step height becomes larger, as previously featured in [58]. This means, at an appreciably large frequency and step height, the whole stack in the step region appears as a semi-infinite medium. The so-called A_i and S_i modes become generalized Lamb waves [50] and lose their symmetry properties. This partly forms the basis for setting the upper limit of the height of the frame steps, introduced in the next chapter.

For the SMR, due to its stratified structure of many layers including the resonating part (top electrode–AlN piezoelectric layer–bottom electrode), the mirror, and the substrate beneath the mirror (Fig. 1.1), the resulting GM is relatively large and hence will not be carried out in the present work. In addition, the behavior of laterally propagating waves in this type of resonator is much more complicated than in the case of FBAR type. Indeed, the q–S wave velocity in AlN is larger than the shear wave velocity in any material in the mirror and substrate below. This leads to the fact that the lateral waves in this device are not really Lamb waves [82]. These waves are identified as generalized Lamb waves and can no longer be categorized as S_i or A_i modes due to the highly antisymmetric structure. FEM simulation is therefore utilized in place of matrix methods for the SMR and consequently, the construction of the fields like \mathbf{u}^{Lamb} , $\mathbf{T}_{3i}^{\text{Lamb}}$, \mathbf{D}^{Lamb} , \mathbf{E}^{Lamb} is limited as a trade-off.

Chapter 3

Design of high-Q BAW resonators using dual-step frame method

3.1 Acoustic Bragg reflector (ABR)

3.1.1 Conventional ABR

An ABR, also known as an acoustic Bragg mirror, comprises alternating layers of high and low acoustic impedance called mirror pairs. It is named after its optical analogue, commonly found in photonic applications such as fiber laser and solid-state bulk laser [84–86]. An ABR functions as a reflector to a chosen acoustic wave, hence coining the phrase “acoustic mirror”, in which each layer typically has a quarter-wavelength thickness, i.e. $\lambda_{TE_1}/4$ for BAW resonators. In an SMR, the ABR is placed underneath the bottom electrode (Fig. 1.1(b)) for the acoustic energy confinement of the TE_1 mode in the piezoelectric layer. The reflectance of an ABR strongly depends on the impedance mismatch between the two layers of the mirror pair and the number of mirror pairs. Indeed, the reflection coefficient of an ABR

that has m mirror pairs is given by [87]

$$R = \frac{Z_{a,0}Z_{a,2}^{2m} - Z_{a,3}Z_{a,1}^{2m}}{Z_{a,0}Z_{a,2}^{2m} + Z_{a,3}Z_{a,1}^{2m}} \quad (3.1)$$

where $Z_{a,0}$, $Z_{a,1}$, $Z_{a,2}$, and $Z_{a,3}$ are, respectively, the specific acoustic impedance of the medium in which the incident wave propagates, the media of the mirror pairs, and the substrate medium. They are defined by

$$Z_a = \rho v_a, \quad (3.2)$$

where ρ is the mass density of the medium and v_a the wave velocity in that medium. This is analogous to the well-known transmission line theory. The behavior of each acoustic mirror layer is similar to the way a transmission line behaves as EM waves propagate in it. It can be seen from (3.1) that R is larger for a larger mismatch between $Z_{a,1}$ and $Z_{a,2}$. Material selection is thus essential for designing an efficient ABR for BAW resonators. Several examples for this significance can be found in [88], [89].

3.1.2 Dual-wave-reflected ABR

At f_r and f_a , more wave modes exist in the bulk of BAW resonators rather than just a single desired TE_1 mode. They are thickness shear (TS) waves (SH, SV) propagating vertically and plate waves (e.g. Lamb waves) propagating laterally in the resonator. If carefully designed, the ABR of an SMR can simultaneously reflect two wavelengths. Indeed, the thicknesses of the mirror layers in an SMR are normally regulated so that it effectively reflects both the TE_1 and TS_1 modes at the frequencies of interest. For most materials, the velocity of shear waves is roughly half of that of the longitudinal waves, i.e. each mirror layer is nearly $\lambda_{TS}/2$ thick. For such a thickness, according to transmission line theory, the TS waves can simply propagate through the ABR and are lost in the substrate beneath. This potentially

Material	v_L (m/s)	v_S (m/s)	Thickness Conventional ABR (nm)	Thickness STM (nm)	Thickness DGM (nm)
Porous SiO ₂	5210	3150	651.3	434.2	1953.8
W	5210	2880	651.3	868.3	3256.3

Table 3.1: Porous SiO₂/W mirror pair thicknesses for various methods, calculated at 2 GHz

lowers the resonator Q factors even if the energy consumed by the shear waves is as small as 1% of the total energy [34], [36], [90]. A dual-wave-reflected ABR therefore plays an important role in minimizing the acoustic leakage through the mirror in an SMR-type resonator.

The design methods for this ABR were previously proposed in [35], introducing the two approaches – stopband theory method (STM) and diffraction grating method (DGM). For the STM, the average velocity ratio between longitudinal and shear waves needs to deviate from 2 by 15% or less to ensure good results. In contrast, the DGM method gives the best results if this ratio deviates from 2 by 15% or more. In addition, the calculated layer thicknesses using both methods are relatively large compared with those in a conventional ABR. For instance, Table 3.1 shows the thicknesses of the porous SiO₂/W pair calculated for various methods. Sputtered porous SiO₂ has a lower Z_a than normal sputtered SiO₂, suitable for the low impedance layer of the mirror [91]. For typical high acoustic impedance materials such as W or Ir, thin film deposition process for large layer thickness could be challenging. In such situation, by systematically varying the layer thicknesses or applying mathematical optimization to the Mason model [30], [92] to find the thicknesses that provide the best reflectance, a combination of thinner layers could be achieved without degrading the robustness of the ABR. However, these methods are relatively more complicated than the two foregoing methods and it is not always assured that they can provide a large dual wave reflectance.

In the present work, the dual-wave-reflected ABR is also laterally applied to both FBAR- and SMR-type resonators in order to alleviate the laterally leaking Lamb

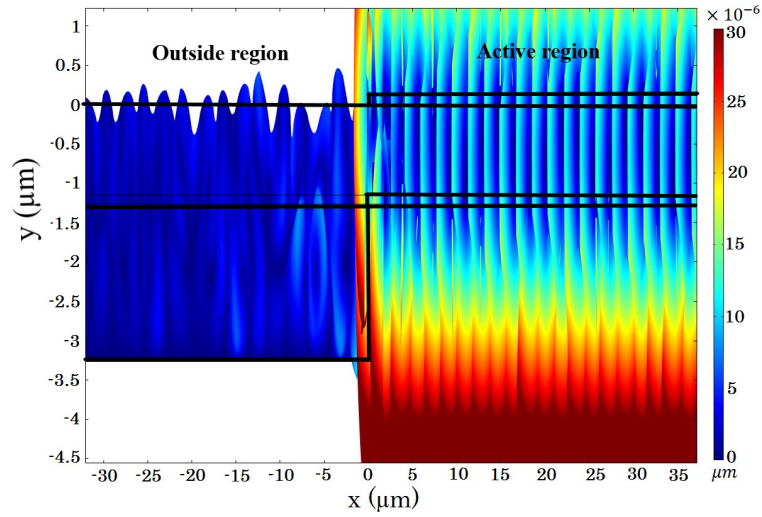


Figure 3.1: Displacement profile of a simulated 2D FBAR at its antiresonance frequency. Only half of the structure is shown due to symmetry.

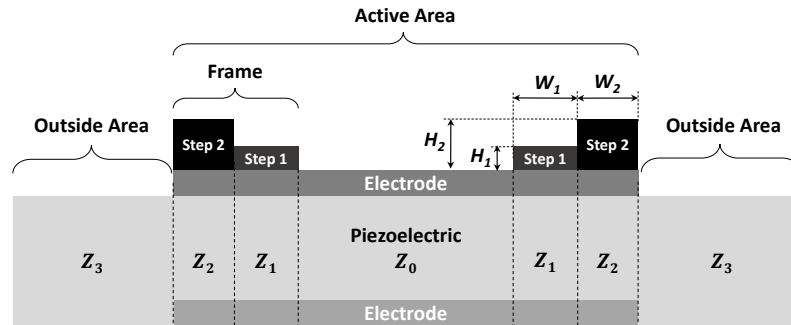


Figure 3.2: 2D schematic of a dual-step frame FBAR.

waves or generalized Lamb waves and further improve the Q factors, especially the one at f_a . More details about this method are presented in the following section.

3.1.3 Dual-step frame method

Fig. 3.1 shows the displacement profile of half a conventional FBAR design at its f_a . The displacement seen in the outside region is the consequence of lateral acoustic

leakage that cannot be neglected in designing high-Q BAW resonators. In fact, it is one of the loss mechanisms that prominently degrades the resonator performance at f_a as previously discussed in [12], [24], [90]. The cause of this loss is addressed to the laterally propagating Lamb waves (in the FBARs) or generalized Lamb waves (in the SMRs). While those losses caused by material viscosity and impurity rely on the material deposition technique and process, this kind of loss is strongly influenced by the resonator geometry. It can be alleviated by implementing a so-called dual-step frame on the periphery of the resonator. This frame is able to reflect the two wave modes that carry the largest amount of energy among the lateral modes. Fig. 3.2 presents a simplified FBAR with such a frame acting as a dual-wave-reflected lateral ABR. By successfully reflecting these wave modes, the Q factors, especially Q_a , are significantly enhanced. In this frame structure, each step is considered as a mirror layer of a lateral ABR. The non-framed, the stepped, and the outside regions are the acoustic waveguides for the laterally propagating waves. The point is that sufficient acoustic impedance mismatch for these lateral waves needs to be created among these regions. By using materials with high mass densities for the two steps, these

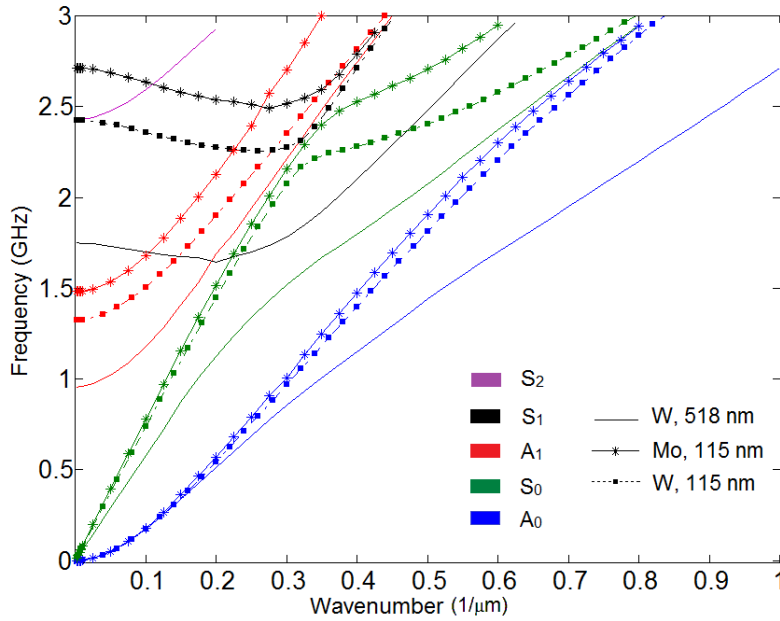


Figure 3.3: Dispersion curves obtained by GM method for the active area of AlN-based FBARs with the same bottom electrode (115 nm W), the same piezoelectric material (1150 nm AlN) and various materials and thicknesses of the top electrode.

mismatches can be achieved following (3.2), except that ρ is now replaced by the average mass density $\bar{\rho}$ of all layers in the stack. The average mass densities of the steps are a crucial key to the success of this method. The reason is that $\bar{\rho}$ needs to be sufficiently large in order to surpass the drop in the wave velocities of the modes of interest as the step height increases. This property can be readily observed in Fig. 3.3, recalling that $v_a = f/k_1$. It highlights the importance of material selection in designing a robust lateral ABR.

For the lateral ABR proposed in the present work, the DGM method is chosen for calculating the step widths W_1 and W_2 shown in Fig. 3.2. Accordingly, each width simultaneously and approximately equals odd multiples of quarter wavelengths $\lambda_{1,2}/4$ of the two lateral waves to be reflected at f_a , or

$$W_i = (2m + 1) \frac{\lambda_{1,i}}{4} = (2n + 1) \frac{\lambda_{2,i}}{4} \quad , \quad i = 1, 2 \quad (3.3)$$

Here m and n are as close to integers as possible.

3.2 Acoustic Poynting vector for piezoelectric media

Acoustic wave fields in solids, though more complicated to analyze, strongly resemble the EM wave fields. The complex Poynting vector, used to quantify the power flow of the waves, is one of the resemblances. For EM waves the well-known complex Poynting vector is defined as

$$\mathbf{P} = \frac{1}{2} (\mathbf{E} \times \mathbf{H}^*) \quad (3.4)$$

where \mathbf{E} is the electrical field and \mathbf{H}^* the complex conjugate of the magnetic field. \mathbf{P} represents the average power flow density during one cycle. Its unit is W/m^2 . The analogous form of \mathbf{P} for acoustic waves in non-piezoelectric media, as derived

in [93], is called complex acoustic Poynting vector. It has the form of

$$\mathbf{P} = -\frac{1}{2}(\mathbf{T} \times \mathbf{v}^*), \quad (3.5)$$

where \mathbf{T} and \mathbf{v} are, respectively, the stress and particle velocity fields of acoustic waves. For piezoelectric media, \mathbf{P} becomes

$$\mathbf{P} = -\frac{\mathbf{T} \times \mathbf{v}^*}{2} - \frac{\phi(j\omega\mathbf{D})^*}{2}, \quad (3.6)$$

where ϕ and \mathbf{D}^* are, respectively, the electrical potential and complex conjugate of the electrical displacement fields, provided that the displacement field has its exponential term of $e^{j(\mathbf{k}\mathbf{x}-\omega\mathbf{t})}$.

The total power flow of a wave mode is found by taking the integral of vector \mathbf{P} over the closed surface normal to its direction. This results in a complex number. Its real part is the real power and its imaginary part the reactive power. For Lamb waves propagating laterally in a stack of three mixed layers as shown in Fig. 2.4, the Poynting vector of each wave mode is parallel to the wave propagation direction (i.e. x_1) and normal to the vertical cross section of the stack. For a simplified 2D stack, the total real power flow P_1 reduces to a line integral over the layer thicknesses and has the unit of W/m. That is

$$P_1 = \text{Re} \left\{ \int_{-h_{M1}-h_{P/2}}^{-h_{P/2}} P_{1,M1} dx_3 + \int_{-h_{P/2}}^{h_{P/2}} P_{1,P} dx_3 + \int_{h_{P/2}}^{h_{M2}+h_{P/2}} P_{1,M2} dx_3 \right\} \quad (3.7)$$

More specifically, for the piezoelectric layer, with the displacement and potential

given in (2.17) and (2.18), $P_{1,P}$ is expanded as

$$\begin{aligned}
 P_{1,P} &= -\frac{1}{2} [T_{1m}v_m^* + \phi(j\omega D_1)^*] = \\
 &= -\frac{1}{2}j\omega \left(\sum_{p=1}^6 F_{mp}^{(1)} C_p e^{jk_3^{(p)}x_3} \sum_{p=1}^6 A_{mp} C_p e^{-jk_3^{(p)}x_3} - \sum_{p=1}^6 A_{4p} C_p e^{jk_3^{(p)}x_3} \sum_{p=1}^6 G_{1p} C_p e^{-jk_3^{(p)}x_3} \right), \\
 m &= \{1, 3\}
 \end{aligned} \tag{3.8}$$

where $v_m = \partial u_m / \partial t$, and the coefficients $F_{mp}^{(1)}$ and G_{1p} are calculated using

$$\begin{aligned}
 G_{1p} &= jk_1 e_{1q1} \sum_{p=1}^6 A_{qp} + j e_{1q3} \sum_{p=1}^6 k_3^{(p)} A_{qp} - jk_1 \varepsilon_{11} \sum_{p=1}^6 A_{4p} - j \varepsilon_{13} \sum_{p=1}^6 k_3^{(p)} A_{4p}, \\
 q &= \{1, 3\}
 \end{aligned} \tag{3.9}$$

and

$$\begin{aligned}
 F_{mp}^{(1)} &= jk_1 c_{1m1n} \sum_{p=1}^6 A_{np} + j c_{1m3n} \sum_{p=1}^6 k_3^{(p)} A_{np} + jk_1 e_{11m} \sum_{p=1}^6 A_{4p} + j e_{31m} \sum_{p=1}^6 k_3^{(p)} A_{4p}, \\
 m, n &= \{1, 3\}.
 \end{aligned} \tag{3.10}$$

Here the superscript ⁽¹⁾ in $F_{mp}^{(1)}$ implies that these are the coefficients for the T_{1m} , $m = \{1, 3\}$ components, distinguishing them from the coefficients F_{mp} for T_{3m} in (2.21) in which the superscript ⁽³⁾ is intentionally omitted for a simpler presentation in the state matrix. Note that the upward and downward q-SH partial waves are excluded in these calculations, hence in (3.8), for example, there are only 6 partial waves in

total. The second term inside the parentheses of (3.7) is afterwards derived as

$$\begin{aligned}
& \int_{-h_P/2}^{h_P/2} P_{1,P} dx_3 = \\
& = -\frac{1}{2}j\omega \int_{-h_P/2}^{h_P/2} \left(\sum_{p=1}^6 \sum_{n=1}^6 F_{mn}^{(1)} C_n e^{jk_3^{(n)} x_3} A_{mp} C_p e^{-jk_3^{(p)} x_3} - \sum_{p=1}^6 \sum_{n=1}^6 A_{4p} C_p e^{jk_3^{(p)} x_3} G_{1n} C_n e^{-jk_3^{(n)} x_3} \right) dx_3 = \\
& = \begin{cases} -\frac{1}{2}j\omega \sum_{p=1}^6 \sum_{n=1}^6 (F_{mn}^{(1)} C_n A_{mp} C_p - A_{4p} C_p G_{1n} C_n) \times \\ \quad \times \frac{1}{j(k_3^{(n)} - k_3^{(p)})} \left[e^{j(k_3^{(n)} - k_3^{(p)}) h_P/2} - e^{-j(k_3^{(n)} - k_3^{(p)}) h_P/2} \right], & n \neq p \\ -\frac{1}{2}j\omega \sum_{p=1}^6 \sum_{n=1}^6 (F_{mn}^{(1)} C_n A_{mp} C_p - A_{4p} C_p G_{1n} C_n) h_P, & n = p \end{cases} \quad (3.11)
\end{aligned}$$

Here $m = \{1, 3\}$. For the electrode layers, the term $\phi(j\omega D)^*$ is eliminated from the integrals, applied for the first and third terms in (3.7).

3.3 A design guideline for high-Q BAW resonators

3.3.1 Material selection

Material selection, as previously mentioned, is a vital step in designing any high performance BAW resonators. For the piezoelectric material, high acoustic velocity, low loss, good thermal conductivity, reliable deposition process, high electromechanical coupling factor k_t , and integrated circuit (IC) integration capability are highly desired. Among common piezoelectric materials like AlN, ZnO, PZT, LiNbO₃, BaTaO₃, and GaN, AlN is the most promising candidate that can fulfill the mentioned requirements [7], [26], [27], [36], [94–96]. AlN is thus the preferred material for BAW manufacturers like Broadcom (holding three quarters of the BAW market), Akoustis (known for its manufacturing process using single crystal AlN that provides superb k_{eff}^2) [97]. More specifically, AlN is mainly found in the commercial FBAR devices. ZnO, on the other hand, is chosen by SMR-type BAW providers like

Material	AlN	W	Ir	Ru	Mo	SiO ₂	Si
$Z_a (\times 10^6 \text{ Pa}\cdot\text{s}/m)$	37.0	100.8	119.6	75.3	64.8	13.6	19.6

Table 3.2: Acoustic impedance values of various materials

Qorvo, TDK. In the present work, AlN [94] is selected as piezoelectric material for both the FBARs and the SMRs.

For the top and bottom metal electrodes, their material(s) must satisfy demanding requirements of conductivity, Z_a , and acoustic loss. For a good confinement of TE₁ mode between the two electrodes, they need to be materials of very high Z_a , yet low sheet resistance in order to reduce ohmic loss. Generally, these characters do not always go hand in hand in one material [7]. However, metals like tungsten (W), molybdenum (Mo), iridium (Ir), ruthenium (Ru), can offer a reasonable compromise and are commonly applied in recent RF BAW devices [12], [29], [32], [46], [98]. In the present simulation, W is chosen for both electrodes of the FBARs and Ir is for those of the SMRs. In addition, due to their excellent Z_a values, they are used as the high impedance layers for the vertical ABR of the SMRs. They are also the selected materials for the frame, owing to their relatively high mass density. For the low impedance layers of the vertical ABR, SiO₂ is the successful candidate regarding its low Z_a and thermal compensation ability. This is based on the fact that SiO₂ has a unique physical property of positive TCF while most other materials have negative ones [99]. Table 3.2 shows a comparison of Z_a (for the TE₁ mode) among various materials, clarifying the selection.

3.3.2 Thickness optimization

The thickness of each layer in a BAW resonator directly influences its resonance frequency and performance. The electrodes need to be sufficiently thick to reduce the bulk resistance that causes ohmic loss in the resonator. The resonator Q_r factor is significantly affected by this kind of loss. However, too thick electrodes relatively to the piezoelectric layer may cause a large degradation of the k_{eff}^2 factor – or

the separation of f_r and f_a – leading to narrower filter bandwidth. Therefore, a proper thickness ratio between the electrodes and piezoelectric layer is required for a satisfying k_{eff}^2 factor [36], [100], [101] while their total thickness must be regulated to obtain the desired resonance frequency. The layer thicknesses in the ABR of an SMR also need to be optimized for dual wave reflection of the TE_1 and TS_1 modes. For instance, Fig. 3.4(b) shows the transmittance of a 7-layer SiO_2/W ABR of an AlN-based SMR that has a Mo top electrode and an Ir bottom electrode. The layer materials and thicknesses are described in Fig. 3.4(a).

3.3.3 Lamb wave characteristics and power flows

In the proposed BAW structures the lateral ABR, or frame, is designed to reflect Lamb waves/generalized Lamb waves. It is thus essential to study the characteristics of these waves beforehand. The dispersions of these waves are plotted for the active regions of the resonators so the type of dispersion (i.e. type I or type II), the cut-off frequencies, and the corresponding wavenumbers in those regions at the desired frequency can be determined. For the FBARs, GM method is carried out and verified

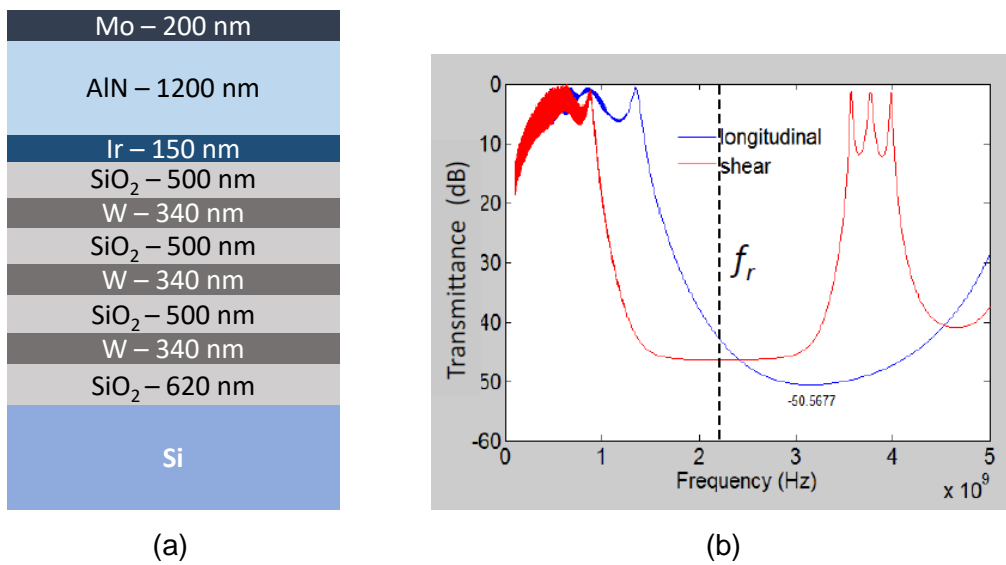


Figure 3.4: Example of an SMR layer stack (a) and the transmittance of its vertical ABR (b).

by FEM results. Afterwards, when u_1^{Lamb} , u_3^{Lamb} , T_{11}^{Lamb} , T_{13}^{Lamb} , ϕ^{Lamb} , and D_1^{Lamb} are found, the mode powers are calculated following (3.7) and two Lamb modes with the largest powers are identified for future steps. For instance, for an FBAR design with W/AlN/W layer stack of 115 nm/1150 nm/115 nm thickness ratio, the two strongest Lamb modes are addressed to the S_{1+} and A_1 modes.

For the SMRs, only FEM simulations are carried out due to the foregoing reasons given in Chapter 2 and the power analyses are consequently excluded. The two strongest lateral modes are assumed to be those with the smallest wavenumbers. It is noted that the DFT applied to the position-dependent simulated FEM displacement data is called the spatial DFT. The resolution of a spatial DFT spectrum depends on either the number of displacement samples in the region of interest or the resonator length. In order to increase the resolution of the dispersion, zero padding technique [102], i.e. adding more zero samples to the original vertical displacement data, could be applied. Increasing the resonator length is not recommended since it leads to cumbersome FEM models that are memory- and time-consuming to simulate.

3.3.4 Frame calculation

The proposed structure has two steps with different heights and widths. The widths are computed from the quarter wavelengths of the lateral modes and are closely related to the step heights. The heights are chosen in such a way that the acoustic impedance mismatches created among the resonator regions are as large as possible. As the step height becomes sufficiently large, an increase in its value results in a smaller drop in Lamb wave velocities. The acoustic impedance of the step region is then decided by the average mass density $\bar{\rho}$. Since the step itself has an impedance considerably higher than that of the fixed-thickness piezoelectric layer, $\bar{\rho}$ is dominated by the step height. It means a larger H_2 value relatively to H_1 (Fig. 3.2) provides a larger acoustic mismatch between the two steps. Nonetheless, the two heights are still limited by the following factors:

- Adequate mismatch needs to be created between the non-framed active region and the first step. This suggests the lower limit for H_1 . Sufficient mismatch between the two steps, on the other hand, predetermines the upper limit for H_1 and lower limit for H_2 .
- At f_a as the height increases, in the step there are more lateral modes to which the total acoustic energy is shared (Fig.3.3). This potentially decreases the efficiency of the frame since it is targeted for reflecting only two modes. The ceiling value of H_2 is thus chosen to limit the number of modes excited in the Step 2 region.
- As discussed at the end of Chapter 2, at a very large H_2 , the lateral waves turns into generalized Lamb waves. They approach Rayleigh-type surface wave on the upper boundary (for S_0 and A_0) or degenerate into vertically-polarized shear waves (for S_1 , A_1 , and higher order modes) in the step medium. Due to the appreciable changes in the nature of these waves and subsequently their complicated behaviors, H_2 is limited to avoid this circumstance.
- Fabrication limitation. Indeed, sputtered metal like W typically undergoes residual stress in the film that builds up with the increased height. This kind of stress, if uncompensated, may cause delamination and failure in the structure [103]. For e-beam evaporated Ir, its low deposition rate requires a long deposition time for thick layers. This may entail failures in the devices due to long exposure to high temperature in the vacuum chamber.

Once the heights are determined, the widths are calculated so that (3.3) is fulfilled. Since m and n in this equation are hardly integers simultaneously, finding the optimum widths might be challenging. In addition, the (m, n) pair preferably holds as smallest value as possible so the frame area is not too large. In fact, the area of the frame has an unwanted yet substantial impact on the resonator performance when its total active area is reduced. This will be further discussed in Chapter 4. In Table 3.3 and Table 3.4 is an example of a step calculation for a W/AlN/W

Step material	Step height H (nm)	λ_{A_1} (nm)	λ_{S_1} (nm)
W	173	2858	2220

Table 3.3: The targeted Lamb modes in the step

m	1	2	3	4	5	6
Calculated n	1.431	2.718	4.005	5.292	6.579	7.866
Rounded n	1	3	4	5	7	8
Step width for the A_1 mode (nm)	2143	3572	5001	6430	7859	9288
Step width for the S_{1+} mode (nm)	1665	3886	4996	6106	8327	9437
Deviation ΔW between two widths (nm)	478	313	5	324	468	149
Chosen width (nm)	\times	\times	5001	\times	\times	\times

Table 3.4: Step width determination

FBAR structure with thickness ratio of 115 nm/1150 nm/115 nm. The chosen reflected Lamb modes are S_{1+} and A_1 since these modes have the largest power at f_a . So λ_1 and λ_2 in (3.3) are respectively λ_{A_1} and $\lambda_{S_{1+}}$. The velocity ratio of these two modes deviates from 2 by less than 15%, proving the DGM method is a reasonable choice [35]. The chosen width is the one that

- results in small ΔW ;
- has relatively small value (compared with the electrode length);
- is the corresponding odd multiple of λ_{A_1} since among the analyzed modes, mode A_1 exhibits a larger acoustic mismatch for the same change of the step height (e.g. see Fig. 8 in *Paper 1*).

3.3.5 Performance evaluation

The designed resonators are evaluated using FEM simulations. The investigated parameters include f_r , f_a , Q_r , Q_a , k_{eff}^2 and the characteristics of electrical impedance Z . For a better visualized comparison of various resonator designs, in several cases, the Q factors are not only calculated at f_r and f_a as formulated in (3.12)

$$Q_{r,a} = \pm \frac{f_{r,a}}{2} \frac{d\angle Z}{df} \bigg|_{f=f_{r,a}}, \quad (3.12)$$

but also for a frequency range using Bode formula [104]

$$Q^{Bode} = -2\pi f \frac{d\angle S_{11}}{d(2\pi f)} \frac{|S_{11}|}{1 - |S_{11}|^2} \quad (3.13)$$

Here $S_{11} = \frac{Z - Z_{ref}}{Z + Z_{ref}}$, known as one of the scattering parameters in an RF network; Z_{ref} is the characteristic impedance, typically holding 50 Ω .

3.4 High-Q BAW resonators

3.4.1 Designed resonators and FEM simulation setups

Fig.3.5 depicts the 2D schematics of both types of BAW resonators with the proposed frame structure where all the materials and dimensions are detailed. Since COMSOL software is utilized to verify the designs, all the relevant simulation setups are also declared. Only 2D simulations are carried out for more efficient use

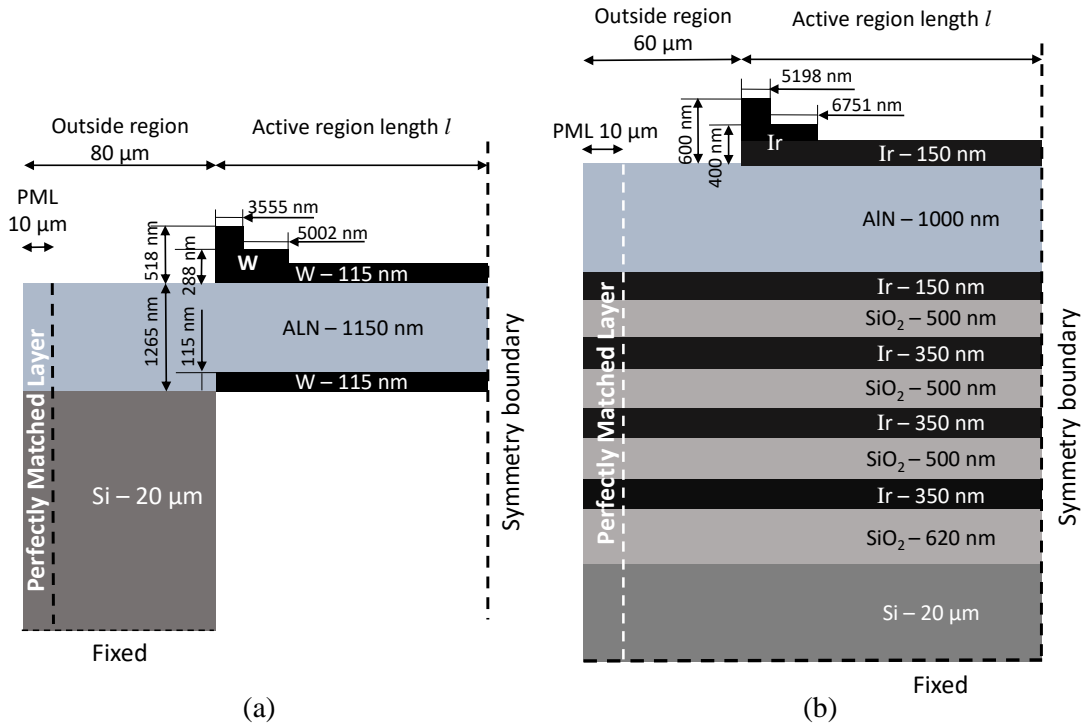


Figure 3.5: High-Q FBAR (a) and SMR (b) designs using the dual-step frame method.

of computer memory and processing time, as recommended in [56]. For calculating the electrical impedance Z , the width of each resonator is assigned a value equal to its length, meaning square resonator. At the outermost edges of the resonators, perfectly matching layers of $10\text{ }\mu\text{m}$ width are applied to avoid artificial reflected waves. Spatial DFT decomposes the vertical displacements into wavenumbers of the existing lateral waves. For facilitating this technique, the regions of interest are uniformly spaced, or sampled. The gridded type of mesh is therefore chosen. The mesh size is one tenth of the smallest wavelength of lateral waves propagating in the structure – that is, 100 nm – to guarantee precise results. Consequently, for a common $100 \times 100\text{ }\mu\text{m}^2$ area of the active region, there would be 1000 elements just along its length. Symmetry boundaries thus becomes a game changer in saving time and computer resources, recalling the fact that all the resonators are horizontally symmetric.

Apart from acoustic loss of all materials and dielectric loss of AlN, ohmic loss caused by electrode resistance is also taken into account. Since this is done by introducing an external resistor in series with the resonator, the part of ohmic loss caused by lateral modes and their induced eddy currents has to be neglected. For a non-framed resonator design, the resistor value is $R_s = 2R_b$ where $R_b = \rho_e l / A$. A is the area of the electrode's cross section, l the length of the active region, and ρ_e the resistivity of the electrode material. For the dual-step frame design, due to the added metal frame, this value reduces to

$$R_s = \rho_e \left[\frac{2W_2}{l(H_2 + t_{el})} + \frac{2W_1}{2W_2(H_2 + t_{el}) + (l - 2W_2)(H_1 + t_{el})} + \frac{l - 2(W_1 + W_2)}{2W_2(H_2 + t_{el}) + 2W_1(H_1 + t_{el}) + t_{el}(l - 2W_1 - 2W_2)} \right] + R_b \quad (3.14)$$

where t_{el} is the thickness of the top electrode in the non-framed region. Other parameters can be found in Fig. 3.2.

3.4.2 Simulation results

The BAW resonators designed with a dual-step frame exhibit a significant enhancement of the Q factors over the frequency range from f_r and f_a , compared with those of the one without a frame and even the one with a single frame. For instance, Fig. 3.6 visualizes the obtained Bode Q values for three different FBAR structures of the same active area ($100 \times 100 \mu\text{m}^2$). More details about the results and the discussions for these FBAR designs can be found in *Paper 1*.

The dual-step frame SMR design also offers better Q factors than do its counterparts single-step frame and non-framed SMRs. For instance, Bode Q values for three different SMR structures, including the one without a frame, the one with a single-step frame, and the one with a dual-step frame with the same active area ($100 \times 100 \mu\text{m}^2$) are shown in Fig. 3.7. The descriptions of these structures are elaborated in *Paper 2*.

3.4.3 Side effects

The obtained simulated results have shown significant enhancements in Q factors of the BAW resonators with the proposed frame designs. The improvements are not only seen at the frequencies of interest, i.e. f_r and f_a , but extendedly for the frequency range between them. However, with the implementation of the frames, of which each step can be considered as a distinct resonator in parallel with the one that provides the main resonance, the k_{eff}^2 factors considerably diminish (Table 3.5). The reason is that these step-resonators have relatively large total areas compared with the active area, and operate at frequencies lower than f_r due to the thickened top metal layer. The larger the step height is, the lower frequency at which the “stepped resonator” resonates will be. Since part of the total energy is shared to these resonators, the effective electromechanical transduction of the main resonator degrades. The second “side effect” is the more pronounced lateral resonances, the so-

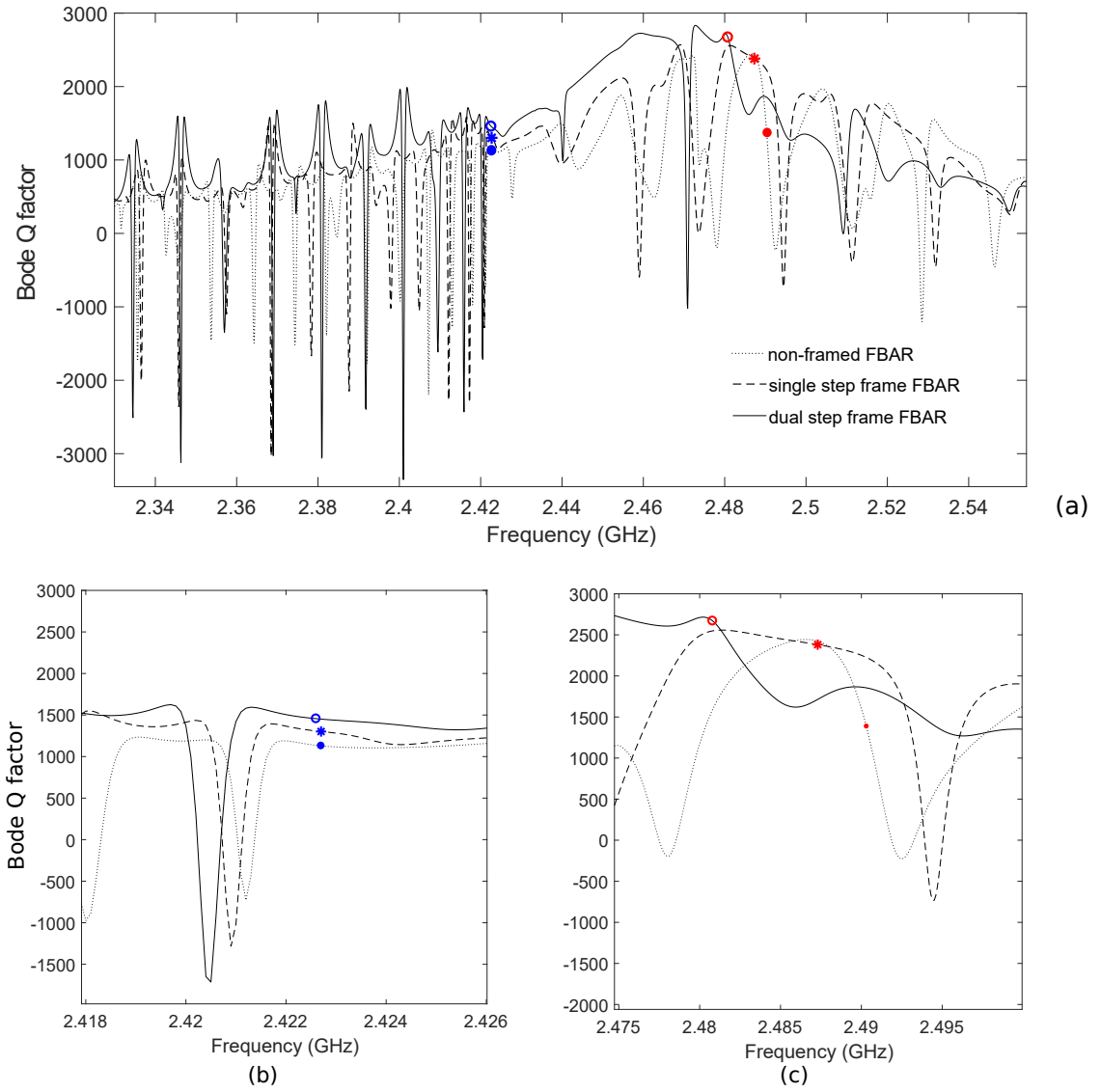


Figure 3.6: Bode Q plots for the three FBAR designs with the same active areas (a) and the narrower frequency range around resonance (b) and antiresonance (c). The dots, circles, and asterisks mark the Q factors at the resonance and antiresonance frequencies of these designs.

called spurious modes, that superimpose on the main resonance and cause stronger ripple in the frequency range of interest. This implies two possibilities. First, more laterally propagating energy is confined in the active region. Second, the lateral standing waves are formed in a smaller area – the non-framed area, leading to larger coupling energy to the spurious modes [45]. Either case shows an implication of the reflection of lateral waves at the frame.

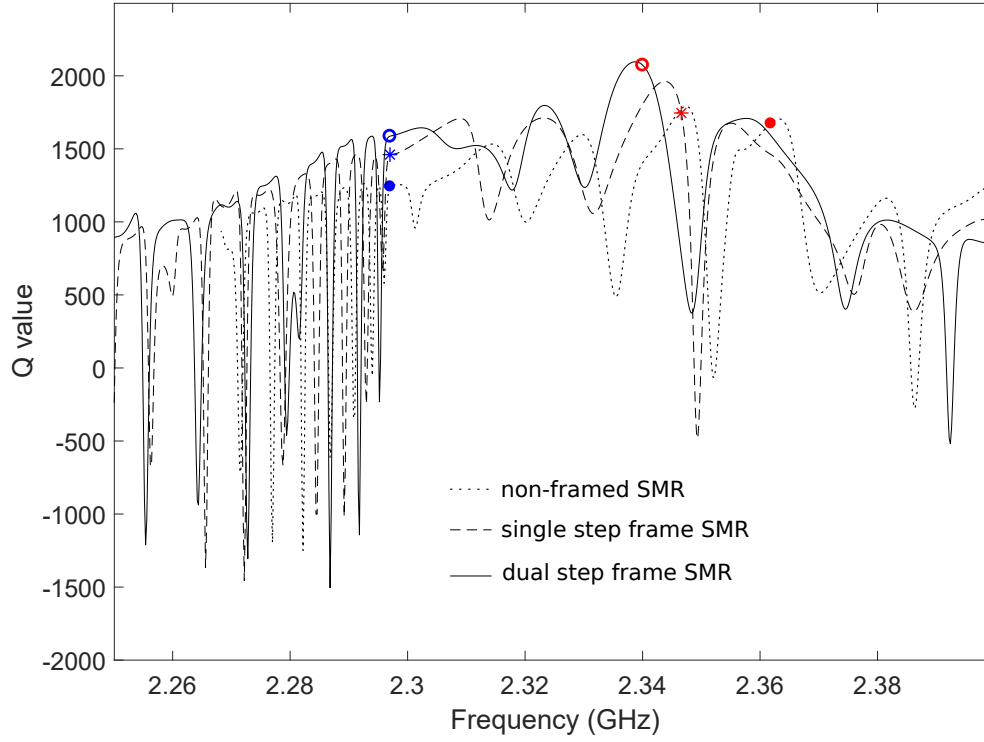


Figure 3.7: Bode plots for various designs of the SMR with similar active areas. The dots, circles, and asterisks mark the Q factors at the resonance and antiresonance frequencies of these designs.

Devices	Parameters	without frame	with single-step frame	with dual-step frame
FBAR	f_r (MHz)	2422.75	2422.70	2422.65
	f_a (MHz)	2490.35	2487.30	2480.80
	k_{eff}^2 (%)	6.52	6.25	5.65
SMR	f_r (GHz)	2297.10	2297.00	2296.90
	f_a (GHz)	2361.80	2351.00	2340.10
	k_{eff}^2 (%)	6.58	5.54	4.47

Table 3.5: Comparisons of results

Chapter 4

The impact of area on BAW resonator performance

4.1 Resonance and antiresonance frequencies affected by transverse behavior of the TE_1 mode

The 1D analyses of the resonator, such as modified Butterworth van Dyke equivalent circuit [105], [106] and Mason model [107], only take into account the pure TE_1 mode and disregard its transverse behavior. Even the 2D matrix methods discussed in Chapter 2, despite the lateral component of the propagation constant being considered, the lateral boundary conditions are ignored. As a result, these methods do not take into account the effects of the lateral dimensions on a resonator's frequency spectrum and performance parameters. Tiersten, in his paper [61], has developed an analysis showing the essential contribution of lateral dimensions to the operation of resonators with rectangular electrodes. His method of analysis is then adopted in the present work for investigating a simplified 2D FBAR structure and its f_r (and f_a) – area dependence. Due to the difference in layer structure between the active region (metal/piezoelectric/metal) and the outside region (piezoelectric/silicon), each of the regions shall have a corresponding dispersion equation that relates the lateral

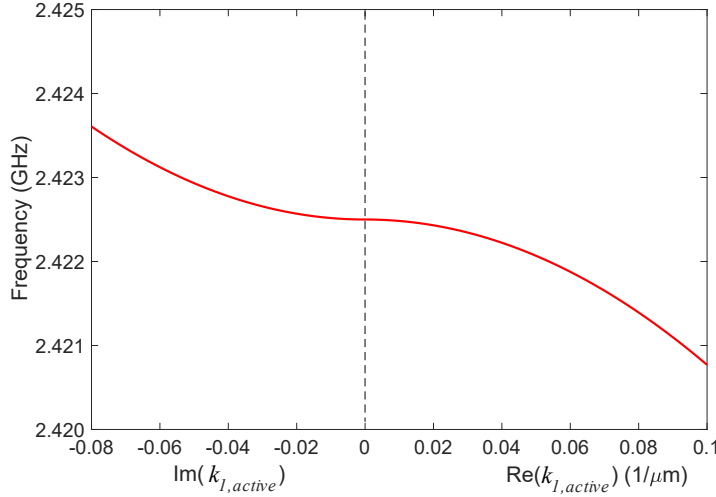


Figure 4.1: Dispersion curves of the S_1 mode in the vicinity of its cut-off frequency (TE_1 resonance) for the active region.

and vertical components of the propagation constant to frequency, such that

$$-\overline{M}_{n\mu}\bar{\xi}_{n\mu}^2 - \bar{c}_{33}^f\bar{\eta}_{nf}^2 + \rho^f\omega^2 = 0 \quad (4.1)$$

$$M_{out,n\mu}\xi_{out,n\mu}^2 - \bar{c}_{33}^f\eta_{out,n}^2 + \rho^f\omega^2 = 0. \quad (4.2)$$

Here, the stiffened stiffness constant $\bar{c}_{33}^f = c_{33}^f + \frac{(e_{33}^f)^2}{\varepsilon_{33}^f}$. The constants $\rho^f, c_{33}^f, e_{33}^f$, and ε_{33}^f are, respectively, the mass density, the stiffness, piezoelectric, and dielectric constants of AlN. $\bar{\xi}_{n\mu}$ and $\xi_{out,n\mu}$ are the lateral components of the n^{th} mode's propagation constant in the layer stack while $\bar{\eta}_{nf}$ and $\eta_{out,n}$ are the vertical components of the propagation constant in the active and outside regions, respectively. The lengthy formulae of the $\overline{M}_{n\mu}$ and $M_{out,n\mu}$ coefficients can be found in [61]. By using an approximation for the lateral BCs, including the continuity of vertical displacement and its first derivation [108], the condition for the laterally propagating mode that has cut-off frequency at the TE_1 resonance frequency (that is, the S_1 mode) to be trapped in the active region is

$$\bar{\xi}_{n\mu} \tan(\bar{\xi}_{n\mu}l) = \xi_{out,n\mu} \quad (4.3)$$

where l is half the top electrode length. This analysis, however, is confined only to part of the S_1 curve close to its cut-off. The term “trapping of wave mode” here implies that the mode laterally propagates in the active region and decays in the outside region, i.e. its energy is confined in the active region. Eq. (4.3) implies that the resonance frequency of a resonator (and its frequency spectrum in general) is greatly influenced by its lateral dimension, especially when it is miniaturized. Fig. 4.2 depicts such a relation. The f_r and f_a values are found by respectively determining the maximum and minimum of the resonator’s electrical admittance. As the electrode length increases, the f_r and f_a curves approach saturation and become independent of the length. The saturated values are identical to those found in the case of pure TE_1 mode, that is, $\bar{\xi}_{n\mu} = 0$ in (4.1). The impact of lateral dimension on the behavior of the TE_1 mode therefore diminishes when the resonator becomes appreciably large. For a small resonator of type II, this impact cannot be ignored since the resonance frequency of the main mode shifts to a value notably smaller than the one obtained from, for example, a 1D model. Note that for type-I resonators, the shift is towards a higher frequency [61]. This finding leads to an essential criterion for miniaturizing a BAW resonator – the lower limit of a resonator lateral dimension at which it still operates at the desired frequency. More

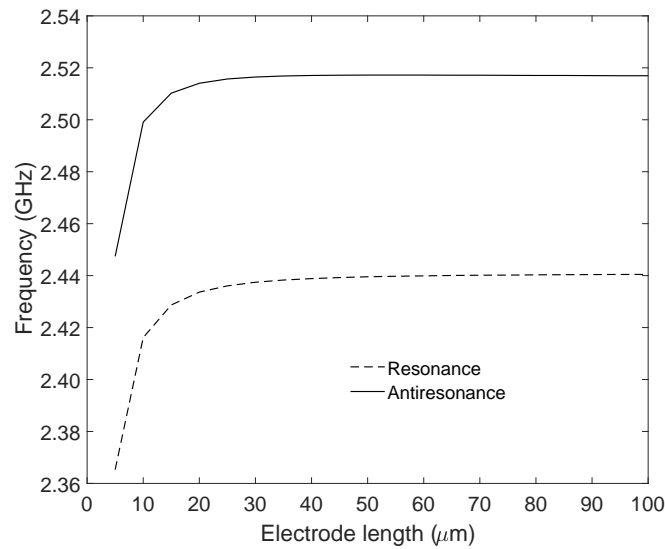


Figure 4.2: Resonance and antiresonance frequencies of a 2D FBAR versus its top electrode length.

importantly, this limit cannot be predicted using either a 1D model or the matrix methods.

4.2 Influence of area on resonator performance

4.2.1 Background

Due to the demanding integration level of the RF front-end modules in mobile handsets, filters and multiplexers are inevitably miniaturized. However, the core resonators can only be reduced to a limited size below which they will no longer function as desired, owing to the significant deterioration of performance parameters. This has been the motivation for further exploring the impact of area on the performance of both BAW resonator types. More specifically, by using 2D FEM simulations the behaviors of the proposed dual-step frame BAW resonators as their size shrinks have been studied. The analyses presented in section 4.1 only focus on the lateral contribution of the TE_1 mode, to the main resonance. 2D FEM, on the other hand, additionally takes into account the involvement of other lateral modes in a large frequency range of interest. It turns out that the resonances of these modes might also affect the Q factors of any resonator that has a realistic area.

4.2.2 FBARs

The resonance of laterally propagating Lamb waves, the so-called spurious modes (Fig. 1.3), accounts for unwanted in-band ripple. These modes occur once their resonance path lengths fit into the resonator. For instance, if the electrode length of a squared FBAR satisfies the half wavelength resonance condition of a Lamb mode at any frequency, i.e.

$$\text{Electrode length } 2l = (2n + 1) \frac{\lambda_{Lamb}}{2} \quad \text{for non-negative integer } n, \quad (4.4)$$

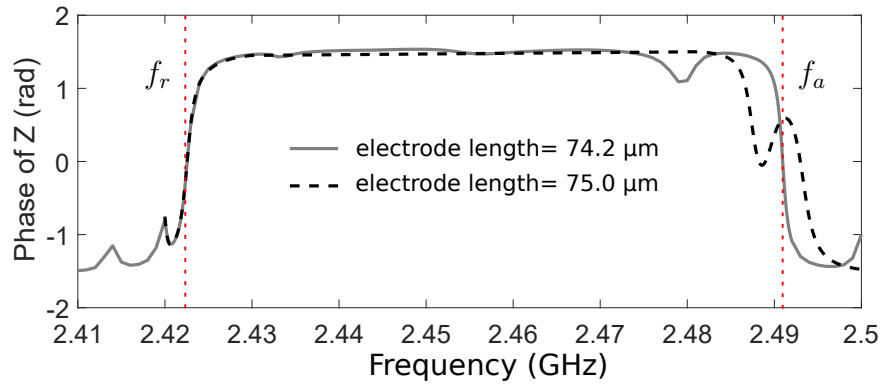


Figure 4.3: Electrical characteristics of two FBARs (without frame design) with various electrode lengths.

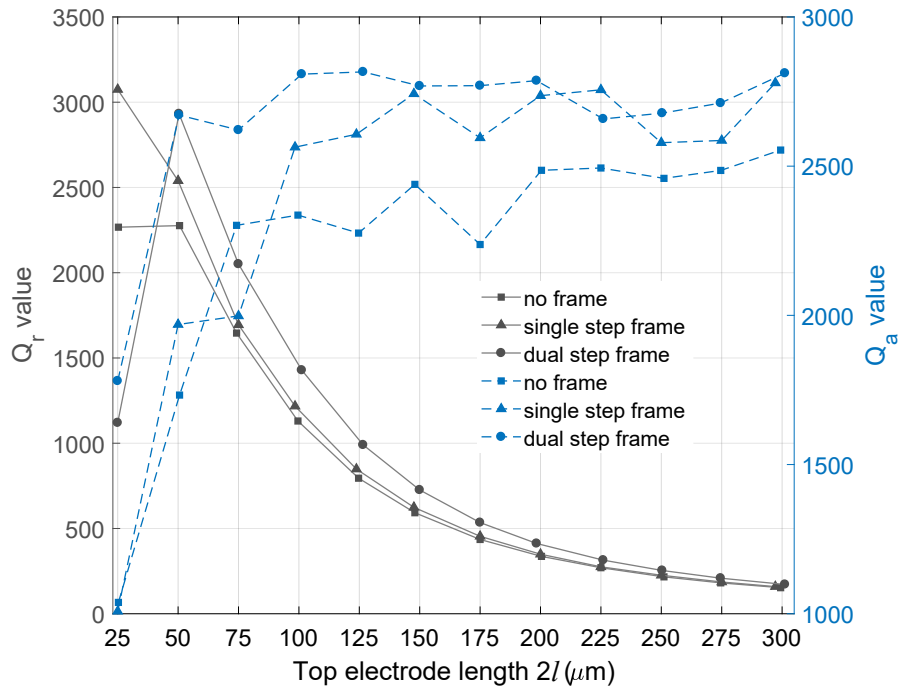


Figure 4.4: Q factors vs electrode length plotted for various FBAR designs. The solid lines are for Q_r and the dashed lines are for Q_a factor.

a spurious mode will occur at that frequency. In an unfortunate situation, (4.4) could be fulfilled at both f_r and f_a , resulting in an undesirable phase change at these frequencies (Fig. 4.3) and consequently, exceedingly diminishing Q_r and Q_a factors [see (3.12)]. Such an incidence can be avoided by slightly adjusting the electrode length so that (4.4) is no longer true at f_r and/or f_a . Since the adjustment is negligible compared to the total length, f_r and f_a are barely affected. For a macroscopic change in the area, e.g. the miniaturization of a squared non-framed FBAR from $100 \times 100 \mu\text{m}^2$ down to $50 \times 50 \mu\text{m}^2$, there is a distinct improvement of

Q_r and a noticeable degradation of Q_a . The former is mostly because the current running through the electrodes decreases with area, leading to a smaller ohmic loss. The latter, on the other hand, is likely because of the dominant lateral wave leakage. The proposed dual-step frame FBAR design has considerably lowered this leakage and enhanced the Q_a factor when the area decreases. In addition, the added metal frame also helps reduce R_s and Q_s is thus improved. This improvement, however, diminishes with the area for $l \gg W_1$ and W_2 , according to (3.14). These behaviors are shown in Fig. 4.4, where the results of a single-step frame FBAR design, which is in accordance to literature [7], is also added for comparison.

4.2.3 SMRs

The performance of an SMR also largely depends on its area. As in the FBAR case, a macro change in the resonator area towards a more miniaturized SMR leads to higher Q_r and lower Q_a . In contrast, a micro change might result in spurious modes at f_r and f_a and worsen both Q_r and Q_a . The dual-step frame design is thus implemented to improve these factors for the miniaturized resonators. The results are presented in Fig. 4.5.

4.2.4 k_{eff}^2 factor of the miniaturized resonators

As expected, one of the main consequences of using the frame on a resonator is the degradation of its k_{eff}^2 factor. For resonators with areas significantly larger than the frame areas, the decrease of k_{eff}^2 is minor. However, when they are miniaturized, the phenomenon could become a vital issue for the applications that require broadband filters [101], [109]. Despite the fact that achieving broad channel bandwidth is not always the case, e.g. the 5G new radio channel bandwidth ranges from a narrow band of 10 MHz to a 100 MHz broadband for the 2.5 GHz range and above [110], k_{eff}^2 of small-sized resonators need to be improved if demanded. In such a situation,

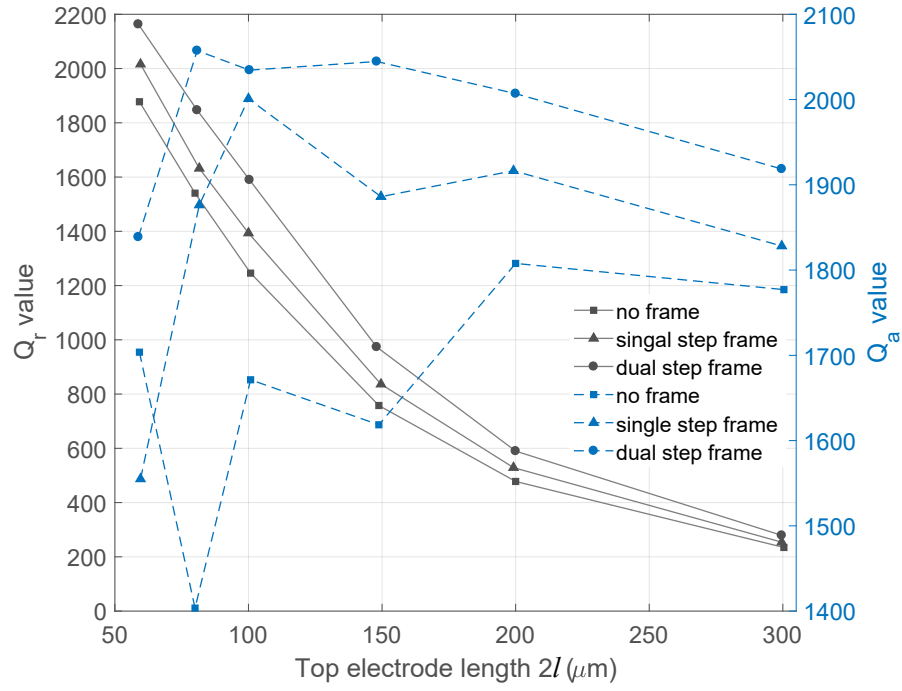


Figure 4.5: Q factors vs electrode length plotted for various SMR designs. The solid lines are for Q_r and the dashed lines are for Q_a factor.

the first suggestion is to find the optimum layer thickness ratio. In addition, single crystal AlN could be an alternative for the piezoelectric layer. The Akoustis company has reported that their BAW resonators using single crystal AlN technology provide far larger k_{eff}^2 than those with the typical polycrystalline AlN [111], [112].

4.2.5 Impact of material quality

As an attempt to investigate the role material quality – in this case the acoustic attenuation – plays in promoting the effectiveness of the dual-step frame BAW resonators. The material quality has been proven to reinforce the efficiency of the proposed designs especially as the resonator size shrinks.

4.3 Microfabrication of the non-framed SMRs

4.3.1 The designed SMRs

This section briefly introduces the fabrication process of the SMRs without a frame. The purpose is to demonstrate the dependence of the SMR performance on its area and shape. The designed SMRs are presented in Table 4.1. In this table, the SiO_2 material used in the acoustic mirror of sample 7WpSiO2 is porous SiO_2 [91], whereas in samples 7WdSiO2 and 5IrdSiO2 the normal SiO_2 is used instead. These SMR structures are, in fact, successively designed so that the latter resonators could overcome the practical limitations that the former ones undergo during the process.

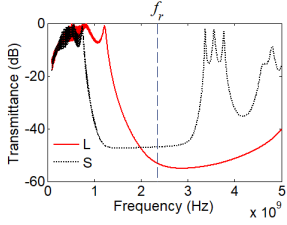
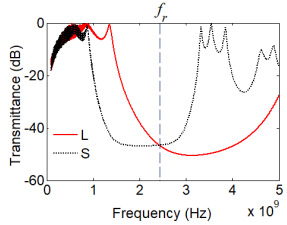
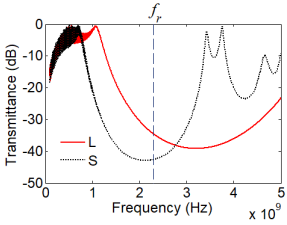
Sample property	7WpSiO2	7WdSiO2	5IrdSiO2
Top 3 layers (bottom to top)	Ir/AlN/Mo 150/1200/150 (nm)	Ir/AlN/Mo 150/1000/200 (nm)	Ir/AlN/Ir 150/1000/140 (nm)
Mirror layers (bottom to top)	$\text{SiO}_2/(\text{W}/\text{SiO}_2) \times 3$ 600/(336/400) $\times 3$ (nm)	$\text{SiO}_2/(\text{W}/\text{SiO}_2) \times 3$ 600/(340/500) $\times 3$ (nm)	$\text{SiO}_2/(\text{Ir}/\text{SiO}_2) \times 2$ 620/(350/500) $\times 2$ (nm)
1D simulated transmission curves of the mirror			

Table 4.1: Various configurations of the fabricated SMRs.

4.3.2 Experimental setups and sample preparation

The SMR mirror layers are deposited atop of 100 mm silicon wafers using pulsed-DC magnetron sputtering technique (for Mo, SiO_2 and W films) and electron beam evaporation (for Ir films). The porous SiO_2 layers (mass density of 2000 kg/m^3) in sample 7WpSiO2 are deposited by sputtering a “pre-cleaned” Si target in a mixed Ar/ O_2 flow in a vacuum chamber. The power applied to the target is 1200 W.

The percentage of O_2 in the gas flow is between 30% and 80%. This setup results in a deposition rate of nearly 100 nm/min [91]. The regular SiO_2 layers in samples 7WdSiO2 and 5IrdSiO2 are achieved with a proper change in the gas percentage and a lower deposition rate (48 nm/min). For the W and Mo targets in the chamber, the DC power is set to 400 W and 200 W with deposition rates of 118 nm and 34 nm per minute, respectively. Unlike other materials, Ir is evaporated from small slugs by an electron beam at 10^{-6} Torr with the substrate kept at 400°C and the deposition rate at 30 nm/min. Before the AlN deposition step (provided by the UPM group), the wafers with Ir bottom electrodes are partitioned into $2 \times 2 \text{ cm}^2$ samples for further processes. AlN piezoelectric films are then sputtered at the rate of 100 nm/min with a 1:5 Ar/ N_2 gas flow, and a pulsed DC power level of 10kW at 400°C in a Sigma fxP cluster tool [29], [113]. It is noted that between two contiguous layers, except for the electrode/AlN interfaces, seed Ti layers of 15–20 nm are necessarily deposited to enhance the adhesion. The top SiO_2 mirror layers are mechanically polished with 0.05 μm Al powder in advance of the deposition of a seed Ti/bottom electrode. They are thus intentionally deposited with an extra thickness of 15–20 nm to compensate for the loss during polishing. The top electrodes are then patterned into arrays of various resonator areas and shapes by wet etching (for Mo) and metal lift-off (for Ir) techniques. In the present work, resonators of both rectangular and elliptical shapes will be measured.

4.3.3 Measurement results

The SMRs in the samples (Fig. 4.6) are characterized by measuring the scattering parameters S_{11} for 30 kHz–3 GHz frequency range. This is done by using an Agilent network analyzer connected to the sample through a ground-signal-ground coplanar RF probe of 200 μm pitch. The data are then converted to electrical impedance Z and fitted to Mason [30] and mBVD equivalent circuits [105] for examining the features (e.g. layer thicknesses, electromechanical coupling constant of AlN) and performance parameters of the resonators.

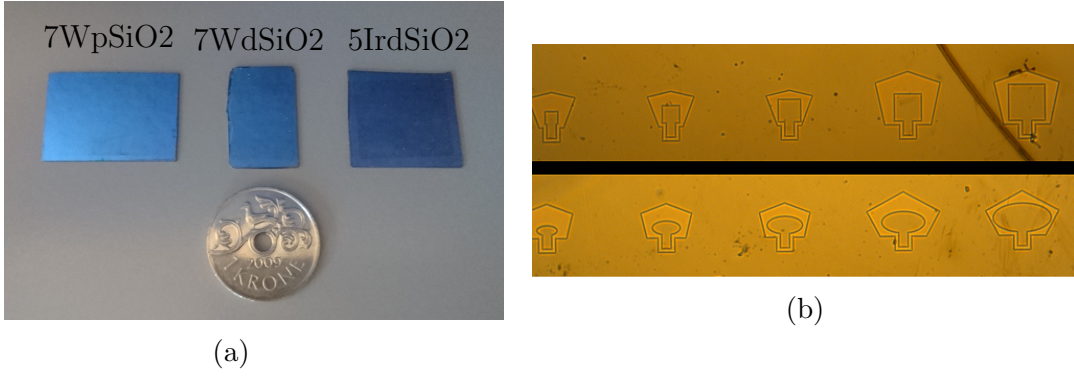


Figure 4.6: Samples under test (a) and the optical microscope images of the fabricated SMRs (b).

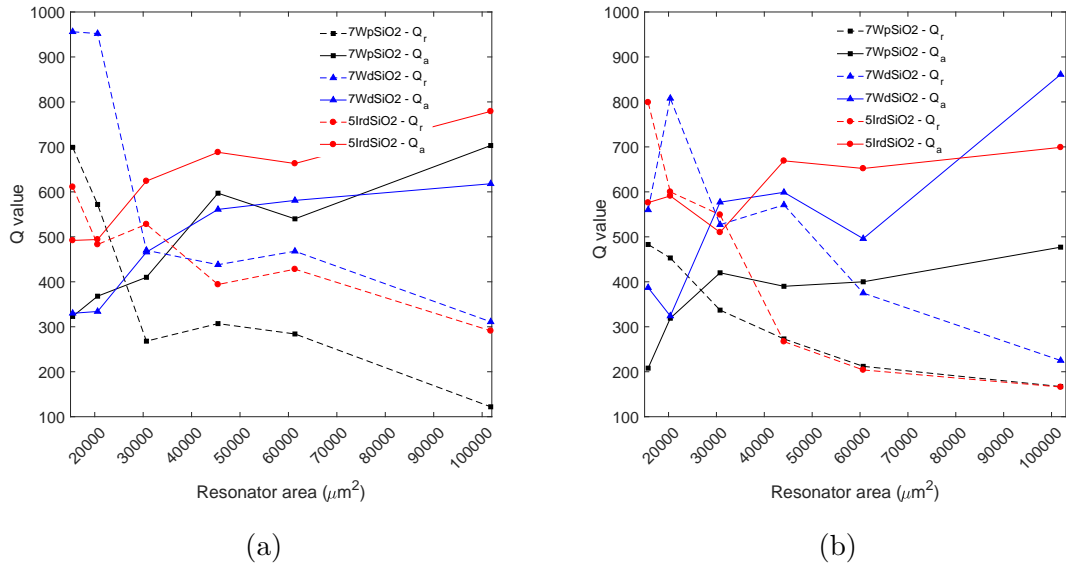


Figure 4.7: Q factor versus area for various SMRs with rectangular (a) and elliptical (b) shapes.

Fig. 4.7 and 4.8 show the results of all samples listed in Table 4.1. As expected, Q_r factors of the samples drastically diminish with resonator area, while the trend is opposite for Q_a and k_{eff}^2 as the area increases. Among the three samples, 7WpSiO2 gives a poorer performance than that of the other two. One possible reason is that porous SiO₂ films fail to reach the desired mass density of 2000 kg/m³. With the setups portrayed in the former subsection, the cathode voltage is, expectedly, around 250 V [91]. The indicator, in fact, reached approximately 310 V when the SiO₂ films in 7WpSiO2 were deposited. This infers that the thicknesses of these porous SiO₂ films may fail to provide an optimum reflection for both longitudinal and shear waves. Normal SiO₂ is thus used in the rest of the samples, in place of porous

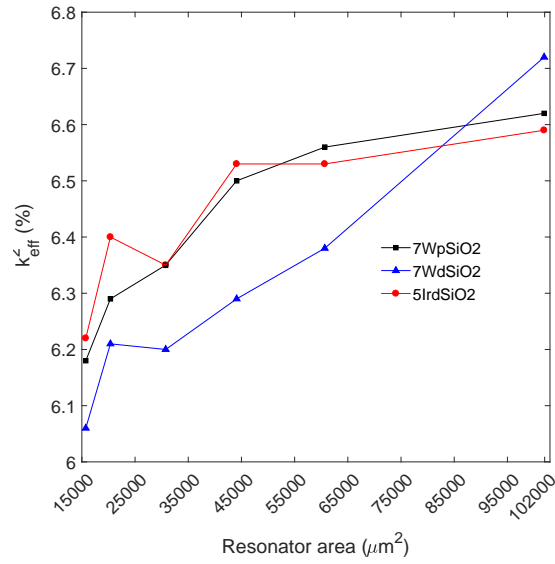


Figure 4.8: k_{eff}^2 versus area plot for various SMR samples.

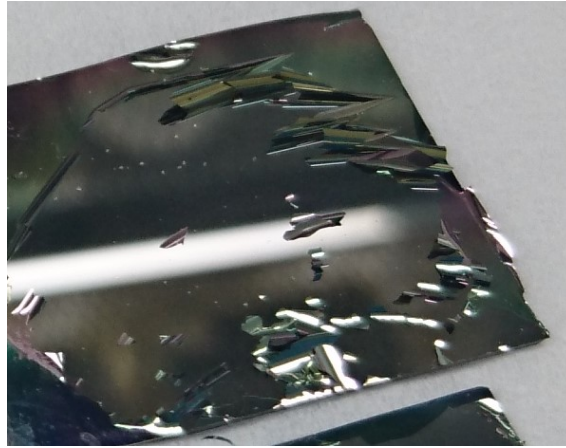


Figure 4.9: Delamination occurring in sample 7WdSiO2.

SiO₂. Sample 7WdSiO₂, on the other hand, undergoes a different technical issue. Sputtered W films are known for their large thickness-dependent residue stress that builds up as more layers are deposited. This causes bending and potential buckling in the multilayered structure. For sample 7WdSiO₂, although the thickness of W films is approximately the one in sample 7WpSiO₂, poor adhesion between normal SiO₂ and stress-borne W layers induces delamination (Fig. 4.9) in half of the sample area. This explains its shape in Fig. 4.6. In sample 5IrdSiO₂, this issue is overcome by the use of Ir for high impedance mirror layers. This sample in general yields slightly better Q_a values than do the others, even though it has fewer mirror layers.

Chapter 5

Conclusions and prospects

5.1 Conclusions

The rapid evolution of mobile communication technology has demanded an enhanced RF acoustic filter technology. Improving the Q factors of the constructed elements of these filters – the BAW resonators – is a key to that enhancement. This thesis presents a novel design method for achieving high- Q BAW resonators. The description dual-step frame method has been coined for the implementation of a two-step frame atop the periphery region of a resonator. Materials with high acoustic impedance are used for these frame structures. Impedance mismatches between the non-frame and step regions and the multiple-quarter-wavelength widths of these steps turn the frame into a lateral Bragg reflector. This inhibits the leakage of laterally propagating acoustic waves (e.g. Lamb waves, generalized Lamb waves) into the outer region of a resonator, hence reducing energy loss and improving the Q factor.

For designing the frame, the characteristics of lateral waves in a mix-multilayered plate are studied using FEM simulations and matrix methods. The calculations for the mode power flows in FBAR-type resonator were conducted by applying acoustic Poynting's theorem. These calculations are not applied to the SMR due to the

complex nature of generalized Lamb waves in a resonator locating on top of a Bragg reflector and a thick substrate. The resonator area – performance relation is also investigated. Apart from enhancing the Q factors for both types of BAW resonators, the proposed frame method reveals the possibility of miniaturizing the resonators for a smaller filter footprint in RF front-end modules.

The key findings of the present work include:

- An explicit design guideline for improving the Q factors of BAW resonators using a dual-step frame. The frame serves as an acoustic Bragg reflector that can laterally reflect the two wave modes that carry the largest amount of energy. It was reported that above the resonance frequency of a type-II (FBAR) resonator, the S_{1+} and S_0 are the two strong modes that cause large spurious resonances [7], [12]. These two modes are symmetric modes and can be measured electrically. The contribution of the antisymmetric modes, on the other hand, was ignored. However, it is proven in this work that the A_1 mode, though it cannot be electrically “seen” in practical measurements, could be as “strong” as the S_{1+} mode and even “stronger” than the S_0 mode. This conclusion is reached by comparing the mode powers, calculated from the Poynting vectors of the lateral modes. By targeting the frame to reflect the two modes S_{1+} and A_1 , the Q_a factor of the optimized resonator is significantly improved. It also provides a better Q_r factor due to a reduction in bulk resistance induced by the metal frame.
- The effect of the resonator lateral edges on the resonance and antiresonance frequencies of the TE_1 mode is also investigated. It is shown that a miniaturized type-II resonator has a lower resonance frequency of its TE_1 mode than that of a large resonator. This occurs due to the contribution of the TE_1 mode’s lateral component to its vertical resonance. This phenomenon, unfortunately, cannot be predicted by such 1D models as Mason model or mBVD circuit. Awareness therefore needs to be raised when designing small-size resonators

using these models.

- One drawback of using 2D FEM simulations for evaluating the resonator performance is also discovered. Namely, if an odd multiple of half-wavelength of any lateral modes fits into the resonator length, spurious resonance occurs. If this happens at f_r or f_a , the corresponding Q factor is strongly affected. This situation should be taken into account during a design procedure.
- The performance parameters, including the Q and k_{eff}^2 factors, largely depend on a resonator area. The Q_a and k_{eff}^2 factors increase with area while the Q_r factor shows an opposite trend. With the use of a dual-step frame, a miniaturized resonator with high Q_r and Q_a can be achieved. However, the resonator size needs to be lower limited to avoid a drastic degradation in the performance parameters.
- The framed resonator undergoes a decrease in k_{eff}^2 factor since the supplied energy is coupled to other resonances of the TE_1 mode propagating in the step regions, apart from the main mode in the non-frame active region. This decrease is more prominent if the frame area is more comparable to the total active area.
- The spurious modes in a framed resonator appear more noticeable than in the one without a frame. This is mainly because of the reduced non-frame active area and the increasing energy coupled to the trapped lateral modes.
- In a practical SMR-type resonator, using W as high acoustic impedance (thick) layers in its vertical Bragg reflector could result in delamination due to accumulated residual stress. Should this occur, Ir is a promising replacement. By optimizing the thickness of the SiO_2 /Ir mirror pair, high reflectance can be obtained for both longitudinal and shear waves, as done in the case of SiO_2 /W pair.

5.2 Prospects

The BAW resonator-based filters play a key role in recent mobile communication technology. In the near future, they will make a substantial contribution to the new mobile technologies, as well as to the development of smart cities and the Internet of Things (IoTs) as the number of handset devices continues to grow. The present work proposes a design guideline for the BAW resonators so that the filters fulfill the demands of such technologies. It is therefore essential to make the prototypes of these optimized resonators, test the proposed method, and estimate the yield when producing them in mass volume. The method also has a potential for applying at a higher range of frequency, namely 5 GHz and above, given that the lateral acoustic leakage is still one of the dominant loss mechanisms in the BAW resonators.

Bibliography

- [1] T. W. Grudkowski, J. F. Black, T. M. Reeder, D. E. Cullen, and R. A. Wagner, “Fundamental Mode VHF/UHF Bulk Acoustic Wave Resonators and Filters on Silicon,” in *1980 Ultrasonics Symposium*, Nov. 1980, pp. 829–833.
- [2] K. M. Lakin and J. S. Wang, “UHF Composite Bulk Wave Resonators,” in *1980 Ultrasonics Symposium*, Nov. 1980, pp. 834–837.
- [3] W. E. Newell, “Tuned integrated circuits: A state-of-the-art survey,” *Proceedings of the IEEE*, vol. 52, no. 12, pp. 1603–1608, Dec. 1964.
- [4] K. M. Lakin, K. T. McCarron, and R. E. Rose, “Solidly mounted resonators and filters,” in *1995 IEEE Ultrasonics Symposium. Proceedings. An International Symposium*, vol. 2, Nov. 1995, pp. 905–908 vol.2.
- [5] K. M. Lakin, “Thin film resonators and filters,” in *1999 IEEE Ultrasonics Symposium. Proceedings. International Symposium*, vol. 2, 1999, pp. 895–906 vol.2.
- [6] S. Mahon and R. Aigner, “Bulk acoustic wave devices—why, how, and where they are going,” in *CS Mantech Conference*, 2007, pp. 15–18.
- [7] K. Hashimoto, Ed., *RF bulk acoustic wave filters for communications*. Artech House, 2009.
- [8] H. Loebl, C. Metzmacher, R. Milsom, P. Lok, F. van Straten, and A. Tuinhout, “RF Bulk Acoustic Wave Resonators and Filters,” *Journal of Electroceramics*, vol. 12, no. 1, pp. 109–118, Jan. 2004.

- [9] M. A. Dubois, “Thin film bulk acoustic wave resonators: a technology overview,” in *MEMSWAVE 03*, Toulouse, France, 2003.
- [10] R. Aigner, “SAW and BAW technologies for RF filter applications: A review of the relative strengths and weaknesses,” in *2008 IEEE Ultrasonics Symposium*, Nov. 2008, pp. 582–589.
- [11] C. C. W. Ruppel, “Acoustic Wave Filter Technology: A Review,” *IEEE Transactions on Ultrasonics, Ferroelectrics, and Frequency Control*, vol. 64, no. 9, pp. 1390–1400, Sep. 2017.
- [12] R. Ruby, “Review and Comparison of Bulk Acoustic Wave FBAR, SMR Technology,” in *2007 IEEE Ultrasonics Symposium Proceedings*, Oct. 2007, pp. 1029–1040.
- [13] R. Aigner, “MEMS in RF-filter applications: thin film bulk-acoustic-wave technology,” in *The 13th International Conference on Solid-State Sensors, Actuators and Microsystems, 2005. Digest of Technical Papers. TRANSDUCERS '05.*, vol. 1, Jun. 2005, pp. 5–8 Vol. 1.
- [14] R. Ruby, P. Bradley, J. D. Larson, and Y. Oshmyansky, “PCS 1900 MHz duplexer using thin film bulk acoustic resonators (FBARs),” *Electronics Letters*, vol. 35, no. 10, pp. 794–795, May 1999.
- [15] C. S. Lam, “A review of the timing and filtering technologies in smartphones,” in *2016 IEEE International Frequency Control Symposium (IFCS)*, May 2016, pp. 1–6.
- [16] R. Ruby and P. Merchant, “Micromachined thin film bulk acoustic resonators,” in *Proceedings of IEEE 48th Annual Symposium on Frequency Control*, Jun. 1994, pp. 135–138.
- [17] R. Aigner, “Acoustic mirror and method for producing the acoustic mirror,” *Acoustical Society of America Journal*, vol. 114, pp. 2533–2533, 2003.

- [18] R. Ruby, “A Snapshot in Time: The Future in Filters for Cell Phones,” *IEEE Microwave Magazine*, vol. 16, no. 7, pp. 46–59, Aug. 2015.
- [19] P. Warder and A. Link, “Golden Age for Filter Design: Innovative and Proven Approaches for Acoustic Filter, Duplexer, and Multiplexer Design,” *IEEE Microwave Magazine*, vol. 16, no. 7, pp. 60–72, Aug. 2015.
- [20] T. Gillenwater, “Evolution of the Smartphone,” *Microwave Journal*, 2017.
- [21] S. Sethi, “FBAR gets excellent reception,” The Langley Group, Tech. Rep., 2015.
- [22] “Global Bulk Acoustic Wave RF Filter Market 2016-2020,” Technavio, Tech. Rep., 2016.
- [23] “GTI 5g device RF component research report,” GTI Group, Tech. Rep., 2018.
- [24] R. Thalhammer and R. Aigner, “Energy loss mechanisms in SMR-type BAW devices,” in *IEEE MTT-S International Microwave Symposium Digest, 2005.*, Jun. 2005.
- [25] R. Thalhammer, G. Fattinger, M. Handtmann, and S. Marksteiner, “Ohmic effects in BAW-resonators,” in *2006 IEEE MTT-S International Microwave Symposium Digest*, Jun. 2006, pp. 390–393.
- [26] A. Ballato and J. G. Gualtieri, “Advances in high-Q piezoelectric resonator materials and devices,” *IEEE Transactions on Ultrasonics, Ferroelectrics, and Frequency Control*, vol. 41, no. 6, pp. 834–844, Nov. 1994.
- [27] P. Muralt, J. Antifakos, M. Cantoni, R. Lanz, and F. Martin, “Is there a better material for thin film BAW applications than AlN?” in *IEEE Ultrasonics Symposium, 2005.*, vol. 1, Sep. 2005, pp. 315–320.
- [28] P. Muralt, “Which is the best thin film piezoelectric material?” Washington DC, 2017.

- [29] M. Clement, J. Olivares, E. Iborra, S. Gozlez-Castilla, N. Rimmer, and A. Rastogi, "AlN films sputtered on iridium electrodes for bulk acoustic wave resonators," *Thin Solid Films*, vol. 42, no. 20, pp. 4673–4678, 2009.
- [30] H. Campanella, *Acoustic Wave and Electromechanical Resonators*. Artech House, 2010.
- [31] M. Rais-Zadeh, V. J. Gokhale, M. Faucher, D. Thron, Y. Cordier, and L. Buchailot, "Gallium Nitride as an Electromechanical Material," *Journal of Microelectromechanical Systems*, vol. 24, no. 1, pp. 249–249, Feb. 2015.
- [32] T. Yokoyama, Y. Iwazaki, Y. Onda, Y. Sasajima, T. Nishihara, and M. Ueda, "Highly piezoelectric co-doped AlN thin films for wideband FBAR applications," in *2014 IEEE International Ultrasonics Symposium*, Sep. 2014, pp. 281–288.
- [33] M. Schneider, M. DeMiguel-Ramos, A. J. Flewitt, E. Iborra, and U. Schmid, "Scandium aluminium nitride-based film bulk acoustic resonators," in *Multidisciplinary Digital Publishing Institute Proceedings*, vol. 1, no. 4, 2017, p. 305.
- [34] S. Marksteiner, J. Kaitila, G. G. Fattinger, and R. Aigner, "Optimization of acoustic mirrors for solidly mounted BAW resonators," in *IEEE Ultrasonics Symposium, 2005.*, vol. 1, Sep. 2005, pp. 329–332.
- [35] S. Jose, A. B. M. Jansman, R. J. E. Hueting, and J. Schmitz, "Optimized reflector stacks for solidly mounted bulk acoustic wave resonators," *IEEE Transactions on Ultrasonics, Ferroelectrics, and Frequency Control*, vol. 57, no. 12, pp. 2753–2763, Dec. 2010.
- [36] J. Kaitila, "Review of Wave Propagation in BAW Thin Film Devices - Progress and Prospects," in *2007 IEEE Ultrasonics Symposium Proceedings*, Oct. 2007, pp. 120–129.

- [37] R. Ruby, J. Larson, J. Feng, and S. Fazzio, “The effect of perimeter geometry on FBAR resonator electrical performance,” in *IEEE MTT-S International Microwave Symposium Digest, 2005.*, Jun. 2005.
- [38] R. Ruby, *Piezoelectric resonator structures and electrical filters.* U.S. Patent 7 629 865, Dec. 2009.
- [39] J. Kaitila, M. Ylilammi, and J. Ell, *Resonator structure and a filter comprising such a resonator structure.* US Patent 6 812 619, Nov. 2004.
- [40] J. Kaitila, M. Ylilammi, J. Ella, and R. Aigner, “Spurious resonance free bulk acoustic wave resonators,” in *IEEE Symposium on Ultrasonics, 2003*, vol. 1, Oct. 2003, pp. 84–87 Vol.1.
- [41] H. Feng, R. S. Fazzio, R. Ruby, and P. Bradley, *Thin film bulk acoustic resonator with a mass loaded perimeter.* US Patent 7 280 007, Oct. 2007.
- [42] T. Jamneala and R. C. Ruby, *Piezoelectric resonator structures and electrical filters having frame elements.* US Patent 8 981 876, Mar. 2015.
- [43] G. G. Fattinger, S. Marksteiner, J. Kaitila, and R. Aigner, “Optimization of acoustic dispersion for high performance thin film BAW resonators,” in *IEEE Ultrasonics Symposium, 2005.*, vol. 2, Sep. 2005, pp. 1175–1178.
- [44] R. Thalhammer, J. Kaitila, S. Zieglmeier, and L. Elbrecht, “4e-3 Spurious Mode Suppression in BAW Resonators,” in *2006 IEEE Ultrasonics Symposium*, Oct. 2006, pp. 456–459.
- [45] T. Pensala and M. Ylilammi, “Spurious Resonance Suppression in Gigahertz-Range ZnO Thin-Film Bulk Acoustic Wave Resonators by the Boundary Frame Method: Modeling and Experiment,” *IEEE Transactions on Ultrasonics, Ferroelectrics, and Frequency Control*, vol. 56, no. 8, pp. 1731–1744, Aug. 2009.
- [46] M. Hara and H. Kuwano, “Spurious Suppression without Energy Dissipation in AluminumNitride-Based Thin-Film Bulk Acoustic Resonator Using Thin Ring

- on Electrode Edge,” *Japanese Journal of Applied Physics*, vol. 51, no. 7S, p. 07GC11, 2012.
- [47] T. Inoue, M. Ohta, and S. Takahashi, “Design of Ultrasonic Transducers with Multiple Acoustic Matching Layers for Medical Application,” *IEEE Transactions on Ultrasonics, Ferroelectrics, and Frequency Control*, vol. 34, no. 1, pp. 8–16, Jan. 1987.
- [48] X. Li, J. Bao, Y. Huang, B. Zhang, G. Tang, T. Omori, and K.-y. Hashimoto, “Use of double-raised-border structure for quality factor enhancement of type II piston mode fbar,” *Microsystem Technologies*, vol. 24, no. 7, pp. 2991–2997, 2018.
- [49] M. Purica, E. Budianu, M. Kusko, and D. Dragoman, “Reflectivity analysis of the bragg reflector based on periodic structures of different thin layers,” in *Electron Devices for Microwave and Optoelectronic Applications, 2003. EDMO 2003. The 11th IEEE International Symposium on*. IEEE, 2003, pp. 296–301.
- [50] B. A. Auld, “Acoustic waves and fields in solids.” New York: John Wiley and Sons, 1990, vol. 2.
- [51] R. C. Ruby, J. D. Larson, R. S. Fazzio, and C. Feng, “Performance degradation effects in FBAR filters and resonators due to lamb wave modes,” in *IEEE Ultrasonics Symposium, 2005.*, vol. 3, Sep. 2005, pp. 1832–1835.
- [52] J. L. Rose, *Ultrasonic Waves in Solid Media*. Cambridge: Cambridge University Press, 1999.
- [53] B. A. Auld, “Acoustic waves and fields in solids.” New York: John Wiley and Sons, 1973, vol. 1, pp. 307–314.
- [54] S. Jose and R. J. E. Hueting, “Experimental investigation of dual wave optimized reflector stacks in solidly mounted resonators,” in *2011 IEEE International Ultrasonics Symposium*, Oct. 2011, pp. 1234–1237.

- [55] B. A. Auld, "Acoustic waves and fields in solids." New York: John Wiley and Sons, 1973, vol. 2, pp. 177–186.
- [56] R. Thalhammer and J. D. Larson, "Finite element analysis of BAW devices: Principles and perspectives," in *2015 IEEE International Ultrasonics Symposium (IUS)*, Oct. 2015, pp. 1–10.
- [57] K. Kokkonen, T. Pensala, and M. Kaivola, "Dispersion and mirror transmission characteristics of bulk acoustic wave resonators," *IEEE Transactions on Ultrasonics, Ferroelectrics, and Frequency Control*, vol. 58, no. 1, pp. 215–225, Jan. 2011.
- [58] D. Royer and E. Dieulesaint, "Elastic Waves in Solids." Springer-Verlag Berlin Heidelberg, 2000, vol. 1, pp. 311–321.
- [59] B. A. Auld, *Acoustic fields and waves in solids*. Krieger publishing company, 1990, vol. II, pp. 32–37.
- [60] T. Jamneala, P. Bradley, A. Shirakawa, R. K. Thalhammer, and R. Ruby, "An Investigation of Lateral Modes in FBAR Resonators," *IEEE Transactions on Ultrasonics, Ferroelectrics, and Frequency Control*, vol. 63, no. 5, pp. 778–789, May 2016.
- [61] H. F. Tiersten and D. S. Stevens, "An analysis of thicknessextensional trapped energy resonant device structures with rectangular electrodes in the piezoelectric thin film on silicon configuration," *Journal of Applied Physics*, vol. 54, no. 10, pp. 5893–5910, 1983.
- [62] W. T. Thomson, "Transmission of Elastic Waves through a Stratified Solid Medium," *Journal of Applied Physics*, vol. 21, pp. 89–93, Feb. 1950.
- [63] N. A. Haskell, "The dispersion of surface waves on multilayered media," *Bulletin of the Seismological Society of America*, vol. 43, no. 1, pp. 17–34, Jan. 1953.

- [64] M. J. S. Lowe, "Matrix techniques for modeling ultrasonic waves in multilayered media," *IEEE Transactions on Ultrasonics, Ferroelectrics, and Frequency Control*, vol. 42, no. 4, pp. 525–542, Jul. 1995.
- [65] S. G. Joshi and Y. Jin, "Propagation of ultrasonic Lamb waves in piezoelectric plates," *Journal of Applied Physics*, vol. 70, pp. 4113–4120, Oct. 1991.
- [66] H. F. Tiersten, "Wave Propagation in an Infinite Piezoelectric Plate," *The Journal of the Acoustical Society of America*, vol. 35, no. 2, pp. 234–239, 1963.
- [67] A. H. Nayfeh, "The general problem of elastic wave propagation in multilayered anisotropic media," *The Journal of the Acoustical Society of America*, vol. 89, no. 4, pp. 1521–1531, 1991.
- [68] E. L. Adler, "Matrix methods applied to acoustic waves in multilayers," *IEEE Transactions on Ultrasonics, Ferroelectrics, and Frequency Control*, vol. 37, no. 6, pp. 485–490, Nov. 1990.
- [69] H. Nowotny and E. Benes, "General onedimensional treatment of the layered piezoelectric resonator with two electrodes," *The Journal of the Acoustical Society of America*, vol. 82, no. 2, pp. 513–521, 1987.
- [70] H. Nowotny, E. Benes, and M. Schmid, "Layered piezoelectric resonators with an arbitrary number of electrodes (general onedimensional treatment)," *The Journal of the Acoustical Society of America*, vol. 90, no. 3, pp. 1238–1245, 1991.
- [71] J. T. Stewart and Y. K. Yong, "Exact analysis of the propagation of acoustic waves in multilayered anisotropic piezoelectric plates," *IEEE Transactions on Ultrasonics, Ferroelectrics, and Frequency Control*, vol. 41, no. 3, pp. 375–390, May 1994.
- [72] L. Knopoff, "A matrix method for elastic wave problems," *Bulletin of the Seismological Society of America*, vol. 54, no. 1, p. 431, 1964.

- [73] H. Schmidt and G. Tango, “Efficient global matrix approach to the computation of synthetic seismograms,” *Geophysical Journal*, vol. 84, pp. 331–359, Feb. 1986.
- [74] G. J. Tango, M. F. Werby, and H. Schmidt, “Global matrix formulation of wave phenomena in plane layered media,” *Mathematical Modelling*, vol. 8, no. Supplement C, pp. 450 – 456, 1987.
- [75] A. K. Mal, “Guided waves in layered solids with interface zones,” *International Journal of Engineering Science*, vol. 26, no. 8, pp. 873 – 881, 1988.
- [76] R. C. Y. Chin, G. W. Hedstrom, and L. Thigpen, “Matrix methods in synthetic seismograms,” *Geophysical Journal*, vol. 77, pp. 483–502, May 1984.
- [77] B. Pavlakovic, M. Lowe, D. Alleyne, and P. Cawley, “Disperse: A General Purpose Program for Creating Dispersion Curves,” in *Review of Progress in Quantitative Nondestructive Evaluation: Volume 16A*, D. O. Thompson and D. E. Chimenti, Eds. Boston, MA: Springer US, 1997, pp. 185–192.
- [78] S. Pant, J. Laliberte, M. Martinez, and B. Rocha, “Derivation and experimental validation of Lamb wave equations for an n-layered anisotropic composite laminate,” *Composite Structures*, vol. 111, no. Supplement C, pp. 566 – 579, 2014.
- [79] D. Kalman, “A singularly valuable decomposition: the SVD of a matrix,” *The college mathematics journal*, vol. 27, no. 1, pp. 2–23, 1996.
- [80] A. Reinhardt, V. Laude, M. Solal, S. Ballandras, and W. Steichen, “Investigation of spurious resonances in thin film bulk acoustic wave resonators,” in *IEEE Ultrasonics Symposium, 2004*, vol. 3, Aug. 2004, pp. 1698–1701 Vol.3.
- [81] D. Alleyne and P. Cawley, “A two-dimensional fourier transform method for the measurement of propagating multimode signals,” *The Journal of the Acoustical Society of America*, vol. 89, no. 3, pp. 1159–1168, 1991.

- [82] C. C. Enz and A. Kaiser, *MEMS-based circuits and systems for wireless communication*. Springer Science & Business Media, 2012.
- [83] M. Sause, “In Situ Monitoring of Fiber-Reinforced Composites,” ser. Springer Series in Materials Science. Springer International Publishing, 2016, no. 242, pp. 196–197.
- [84] A. Abdolvand, K. G. Wilcox, T. K. Kalkandjiev, and E. U. Rafailov, “Cone-refrangent solid-state bulk laser,” in *The European Conference on Lasers and Electro-Optics*. Optical Society of America, 2009, p. CA.P41.
- [85] M. F. Schubert, J.-Q. Xi, J. K. Kim, and E. F. Schubert, “Distributed bragg reflector consisting of high-and low-refractive-index thin film layers made of the same material,” *Applied Physics Letters*, vol. 90, no. 14, p. 141115, 2007.
- [86] L. A. Coldren, G. Fish, Y. Akulova, J. Barton, L. Johansson, and C. Coldren, “Tunable semiconductor lasers: A tutorial,” *Journal of Lightwave Technology*, vol. 22, no. 1, p. 193, 2004.
- [87] C. Sheppard, “Approximate calculation of the reflection coefficient from a stratified medium,” *Pure and Applied Optics: Journal of the European Optical Society Part A*, vol. 4, no. 5, p. 665, 1995.
- [88] T. Pensala, *Thin Film Bulk Acoustic Wave Devices*. VTT Publications, 2011, pp. 32–37.
- [89] J. Olivares, E. Wegmann, M. Clement, J. Capilla, E. Iborra, and J. Sangrador, “Wide bandwidth bragg mirrors for multi-band filter chips,” in *Ultrasonics Symposium (IUS), 2009 IEEE International*. IEEE, 2009, pp. 2119–2122.
- [90] K. Hashimoto, Ed., *RF bulk acoustic wave filters for communications*. Artech House, 2009, pp. 78–81.
- [91] J. Olivares, E. Wegmann, J. Capilla, E. Iborra, M. Clement, L. Vergara, and R. Aigner, “Sputtered SiO₂ as low acoustic impedance material for bragg

- mirror fabrication in BAW resonators,” in *Frequency Control Symposium, 2009 Joint with the 22nd European Frequency and Time forum. IEEE International*. IEEE, 2009, pp. 316–321.
- [92] D. Royer and E. Dieulesaint, *Elastic waves in solids II: generation, acousto-optic interaction, applications*. Springer Science & Business Media, 1999.
- [93] B. A. Auld, *Acoustic fields and waves in solids*. Krieger publishing company, 1990, vol. I, ch. 5.
- [94] J. G. Gualtieri, J. A. Kosinski, and A. Ballato, “Piezoelectric materials for acoustic wave applications,” *IEEE Transactions on Ultrasonics, Ferroelectrics, and Frequency Control*, vol. 41, no. 1, pp. 53–59, Jan. 1994.
- [95] M. Rais-Zadeh, V. J. Gokhale, A. Ansari, M. Faucher, D. Théron, Y. Cordier, and L. Buchaillot, “Gallium nitride as an electromechanical material,” *Journal of Microelectromechanical Systems*, vol. 23, no. 6, pp. 1252–1271, 2014.
- [96] E. Savrun, V. Nguyen, and D. Abe, “High thermal conductivity aluminum nitride ceramics for high power microwave tubes,” in *Vacuum Electronics Conference, 2002. IVEC 2002. Third IEEE International*. IEEE, 2002, pp. 34–35.
- [97] L. Gwennap, “Akoustis challenges broadcom FBAR.” Linley newsletter, 2016.
- [98] M. Ueda, T. Nishihara, S. Taniguchi, T. Yokoyama, J. Tsutsumi, M. Iwaki, and Y. Satoh, “Film bulk acoustic resonator using high-acoustic-impedance electrodes,” *Japanese Journal of Applied Physics*, vol. 46, no. 7S, p. 4642, 2007.
- [99] H. Yu, W. Pang, H. Zhang, and E. S. Kim, “Ultra temperature-stable bulk-acoustic-wave resonators with sio₂ compensation layer,” *IEEE transactions on ultrasonics, ferroelectrics, and frequency control*, vol. 54, no. 10, 2007.
- [100] J. Verdu, P. de Paco, and O. Menendez, “Electric equivalent circuit for the thickened edge load solution in a bulk acoustic wave resonator,” *Progress in Electromagnetics Research*, pp. 13–23, 2010.

- [101] K. Lakin, J. Belsick, J. McDonald, and K. McCarron, "Improved bulk wave resonator coupling coefficient for wide bandwidth filters," in *Ultrasonics Symposium, 2001 IEEE*, vol. 1. IEEE, 2001, pp. 827–831.
- [102] F. Lindsten, "A remark on zero-padding for increased frequency resolution," 2010.
- [103] P. Waters and A. A. Volinsky, "Stress and Moisture Effects on Thin Film Buckling Delamination," *Experimental Mechanics*, vol. 47, no. 1, pp. 163–170, Feb. 2007.
- [104] D. A. Feld, R. Parker, R. Ruby, P. Bradley, and S. Dong, "After 60 years: A new formula for computing quality factor is warranted," in *Ultrasonics Symposium, 2008. IUS 2008. IEEE*. IEEE, 2008, pp. 431–436.
- [105] J. D. Larson, P. D. Bradley, S. Wartenberg, and R. C. Ruby, "Modified Butterworth-Van Dyke circuit for FBAR resonators and automated measurement system," in *2000 IEEE Ultrasonics Symposium. Proceedings. An International Symposium (Cat. No.00CH37121)*, vol. 1, Oct. 2000, pp. 863–868 vol.1.
- [106] H. Jaffe, D. Berlincourt, T. Kinsley, T. Lambert, D. Schwartz, E. Gerber, and I. Fair, "Ire standards on piezoelectric crystals: measurements of piezoelectric ceramics," *Proc. IRE*, vol. 49, no. 1161-1169, pp. 17–09, 1961.
- [107] W. P. Mason and H. Baerwald, "Piezoelectric crystals and their applications to ultrasonics," *Physics Today*, vol. 4, p. 23, 1951.
- [108] H. Tiersten, *Linear piezoelectric plate vibrations: elements of the linear theory of piezoelectricity and the vibrations of piezoelectric plates*. Plenum Press, 1969.
- [109] Q. Chen and Q.-M. Wang, "The effective electromechanical coupling coefficient of piezoelectric thin-film resonators," *Applied Physics Letters*, vol. 86, no. 2, p. 022904, 2005.

- [110] “TS 38.101-1 v1.0.0 on NR; user equipment (UE) radio transmission and reception; part 1: Range 1 standalone,” Qualcomm, 12-2017.
- [111] J. B. Shealy, J. B. Shealy, P. Patel, M. D. Hodge, R. Vetury, and J. R. Shealy, “Single crystal aluminum nitride film bulk acoustic resonators,” in *2016 IEEE Radio and Wireless Symposium (RWS)*, Jan. 2016, pp. 16–19.
- [112] J. B. Shealy, R. Vetury, S. R. Gibb, M. D. Hodge, P. Patel, M. A. McLain, A. Y. Feldman, M. D. Boomgarden, M. P. Lewis, B. Hosse *et al.*, “Low loss, 3.7 ghz wideband baw filters, using high power single crystal aln-on-sic resonators,” in *Microwave Symposium (IMS), 2017 IEEE MTT-S International*. IEEE, 2017, pp. 1476–1479.
- [113] J. Olivares, M. Clement, E. Iborra, S. Gonzalez-Castilla, N. Rimmer, and A. Rastogi, “Assessment of aluminum nitride films sputtered on iridium electrodes,” in *Ultrasonics Symposium, 2007. IEEE*. IEEE, 2007, pp. 1401–1404.

List of papers omitted from online edition due to publisher's restrictions

Papers included in the thesis

1. **N. Nguyen**, A. Johannessen, S. Rooth, and U. Hanke, “A design approach for high-Q FBARs with a dual step frame”, *Transactions on Ultrasonics Ferroelectrics and Frequency Control*, vol. 65, 2018, pp. 1717–1725.
2. **N. Nguyen**, A. Johannessen, S. Rooth, and U. Hanke, “The impact of area on BAW resonator performance and an approach to device miniaturization”, accepted to be published in *Ultrasonics* journal.
3. **N. Nguyen**, S. Rooth, A. Johannessen, and U. Hanke, “Improvement of methods in analyzing the propagation of plate waves in FBARs” in 2016 IEEE International Frequency Control Symposium (IFCS), 2016, pp. 1–6.
4. **N. Nguyen**, A. Johannessen, and U. Hanke, “Design of high-Q thin film bulk acoustic resonator using dual-mode reflection” in 2014 IEEE International Ultrasonics Symposium, 2014, pp. 487–490.
5. **N. Nguyen**, S. Rooth, A. Johannessen, and U. Hanke, “Geometrically optimized FBAR elements for ladder type filter”, proceeding of International Workshop on Microwave Filters, CNES/ESA, 2015.

The present work was also presented at the following workshops and seminars (without proceedings)

6. **N. Nguyen**, S. Rooth, A. Johannessen, and U. Hanke, “Inhibiting laterally leaking Lamb waves in thin film bulk acoustic resonators”, presented at Scandinavian Symposium on Physical Acoustics, Geilo, 2018.
7. **N. Nguyen**, A. Johannessen, S. Rooth, and U. Hanke, “The effects of area on the performance of solidly mounted resonators”, presented at IC1208 MCM7 & WG meeting, Luxembourg, 2017.
8. **N. Nguyen**, A. Johannessen, S. Rooth, and U. Hanke, “A new design method for the improvement of FBAR quality factor at anti-resonance frequency”, presented at IC1208 MCM7 & WG meeting, Vilnius, 2016.